

MIU²Net: weak-lensing mass inversion using deep learning with nested U-structures*

Han W.G.¹, An Zhao², Xingyue Chen³, Ran Li¹, Rui Li⁴, Xiangkun Liu², Zhao Chen⁵ and Yu Yu⁵

¹ School of Physics and Astronomy, Beijing Normal University, Beijing 100875, China

² South-Western Institute for Astronomy Research, Yunnan University, Kunming 650500, China

³ School of Astronomy and Space Science, University of Chinese Academy of Sciences, Beijing 100049, China

⁴ Institute for Astrophysics, School of Physics, Zhengzhou University, Zhengzhou, 450001, China

⁵ Department of Astronomy, School of Physics and Astronomy, Shanghai Jiao Tong University, Shanghai 200240, China

Abstract One of the primary goals of next-generation gravitational lensing surveys is to measure the large-scale distribution of dark matter, which requires accurate mass inversion to convert weak-lensing shear maps into convergence (κ) fields. This work develops a mass inversion method tailored for upcoming space missions such as CSST and *Euclid*, aiming to recover both the mass distribution and the convergence power spectrum with high fidelity. We introduce MIU²Net, a versatile deep-learning framework for κ -map reconstruction based on the U²-Net architecture. A new loss function is constructed to jointly estimate the convergence field and its frequency-domain energy distribution, effectively balancing optimal mean squared error and optimal power-spectrum recovery. The method incorporates realistic observational effects into shear fields, including shape noise, reduced shear, and complex masks. Under noise levels anticipated for future space-based lensing surveys, MIU²Net recovers the convergence power spectrum with 4% uncertainties up to $l \simeq 500$, significantly outperforming Wiener filtering and MCALens. Beyond two-point statistics, the method accurately reconstructs the convergence distribution, peak centroid, and peak amplitude. Compared to other learning-based approaches such as DeepMass, MIU²Net reduces the root-mean-square error by 5% without smoothing and by 38% with a 1-arcmin smoothing scale. MIU²Net represents a substantial advancement in mass inversion methodology, offering improved accuracy in both RMSE and power-spectrum reconstruction. It provides a promising tool for mapping dark matter environments and large-scale structures in the era of next-generation space lensing surveys.

Key words: gravitational lensing: weak – methods: statistical – dark matter – large-scale structure of Universe

1 INTRODUCTION

Gravitational lensing is the relativistic bending of light as it travels to us. The degree of bending depends on the gravitational potential of intervening mass, as well as the geometry of the lensing system. In the weak lensing regime, we study the distortions in background galaxy shapes to infer the foreground mass distribution through which light travels. Weak lensing information can be accessed by two equivalent fields: the (reduced) shear field¹ $\gamma_{1,2}$ and the convergence field κ . The (reduced) shear field is an observable that describes the stretching of galaxy shapes. The

convergence field, however, is not an observable, but it is directly linked to the projected matter density. The convergence field has extensive applications in large-scale structure identification (e.g. Davies et al. 2018; Mead et al. 2010; Tam et al. 2020), constraining the cosmological model (e.g. Liu et al. 2015; Davies et al. 2021; Liu & Madhavacheril 2019), studies of non-Gaussianity in the universe (e.g. Pires et al. 2020), and tests of gravity (e.g. Liu et al. 2016; Ling et al. 2015). Therefore, a transformation from $\gamma_{1,2}$ field to κ field is much desired. This transformation is typically referred to as a “mass inversion” because we are recovering mass distribution from observed shear.

However, mass inversion is an ill-posed inverse problem due to an excessive amount of noise. It is well known that the intrinsic shape dispersion of galaxies (known as “shape noise,” see Sect. 2.2) is much more significant than the typical distortion from weak lensing. Moreover,

* All python code and data that we used to generate the figures in the paper are available at <https://github.com/MIU2NET/miu2net>.

¹ For a detailed discussion of the shear and the reduced shear, please refer to the end of Sect. 2.1.

the observed shear map is pixelated and sampled at discrete locations; it also has empty regions because of survey geometry, bright star masks, CCD defects, etc. We also cannot know the mean convergence due to a fundamental limit called the mass-sheet degeneracy (Falco et al. 1985; Schneider & Seitz 1995; Bradač et al. 2004). These observational limitations further complicate mass inversion. Starting with Kaiser & Squires (1993), many mass inversion techniques have been proposed, including Kaiser-Squires (KS) deconvolution and its variants (Kaiser & Squires 1993; Pires et al. 2009; Deriaze et al. 2012; Pires et al. 2020), Wiener filtering (Gaussian prior) (Lahav et al. 1994; Zaroubi et al. 1995), sparsity prior (Lanusse et al. 2016; Jeffrey et al. 2018; Price et al. 2021), and Bayesian methods with other physically motivated priors (Jasche & Wandelt 2013; Porqueres et al. 2021; Fiedorowicz et al. 2022), all assuming mean convergence of zero. Additionally, Starck et al. (2021) proposed an iterative approach (MCALens) by combining Wiener filtering with a sparsity-based non-Gaussian component. With the rapid rise of machine learning, mass inversion based on deep learning techniques started to flourish. Jeffrey et al. (2020) pioneered this interdisciplinary work by designing DeepMass, a UNet convolutional neural network (CNN) for DES mass inversion. Hong et al. (2021) applied the CNN architecture on galaxy clusters, and Shirasaki et al. (2019) used variants of generative adversarial network (GAN) to denoise convergence maps. However, despite the visual competitiveness of deep learning reconstructions, all proposed CNN models minimize only a pixel-wise loss function, thereby limiting the physical significance of CNN-based convergence maps. GAN variants are different in that they include learned networks as parts of the loss function, but they too only optimize in the spatial domain. Specifically, Shirasaki et al. (2019) show that the classical conditional GAN model (pix2pix; Isola et al. 2017) has limited capacity in Fourier space, yielding a sub-optimal estimate of the convergence power spectrum.

Building on previous works (Jeffrey et al. 2020; Hong et al. 2021; Shirasaki et al. 2019), we propose a versatile deep learning framework for mass inversion (MIU²Net) based on a nested U-shaped CNN. We construct a new loss function to jointly estimate the convergence field and its frequency domain energy distribution, seeking a balance between optimal MSE and optimal power spectrum. Under a noise level achievable by upcoming space lensing surveys, we find that MIU²Net recovers the convergence power spectrum with 4% uncertainties up to $l \simeq 500$, 1060% more accurate than Wiener filtering and 930% more accurate than MCALens with optimal power spectrum. MIU²Net can also recover the convergence distribution, peak centroid, and peak abundance. A visual

comparison between MIU²Net, Kaiser-Squires deconvolution (KS), Wiener filtering (WF), MCALens (MCA), and SimpleUNet (UNet, based on DeepMass) is shown in Fig. 1. We introduce the details of the method and results in this paper.

The structure of this paper is as follows. In Sect. 2, we introduce the basic formalism of weak gravitational lensing as well as the major challenges in mass inversion such as shape noise, mass-sheet degeneracy, and missing data. In Sect. 3, we briefly outline the current mass inversion methods including KS, WF, and UNet. We introduce our method, MIU²Net, in Sect. 4, detailing our training data, network architecture, and loss function. We demonstrate the reconstruction results in Sect. 5 and compare the MIU²Net results to unsupervised methods such as KS, WF, MCA, and supervised deep learning methods such as UNet.

2 WEAK GRAVITATIONAL LENSING

2.1 Formalism

In this section, we introduce the basics of weak lensing formalism and the observational challenges it faces. (For a detailed review of weak lensing formalism, please see Bartelmann & Schneider 2001; Mandelbaum 2018.) Consider the 2D lensing potential $\psi(\theta)$ that encodes the deflection of light rays. The reduced (scaled) deflection angle α can be written as the gradient of the potential

$$\alpha = \nabla \psi, \quad (1)$$

and the convergence κ is related to ψ through the 2D Poisson equation

$$\kappa = \frac{1}{2} (\partial_1^2 + \partial_2^2) \psi = \frac{1}{2} \nabla^2 \psi, \quad (2)$$

where the subscripted partial derivatives ∂_1, ∂_2 relates to the two angular coordinates θ_1, θ_2 on the celestial sphere. The two-component shear is expressed as a complex field, where each component is described by ψ as

$$\gamma_1 = \frac{1}{2} (\partial_1^2 - \partial_2^2) \psi, \quad \gamma_2 = \partial_1 \partial_2 \psi, \quad (3)$$

and the complex shear field

$$\gamma = \gamma_1 + i\gamma_2 = |\gamma| e^{2i\varphi}. \quad (4)$$

Note that all lensing quantities can be derived from the lensing potential ψ , thereby setting the relations between them. Through the lensing potential, we can express complex shear in terms of a convolution on the convergence, or

$$\gamma(\theta) = \frac{1}{\pi} \int_{\mathbb{R}^2} d^2\theta' \mathcal{D}(\theta - \theta') \kappa(\theta'), \quad (5)$$

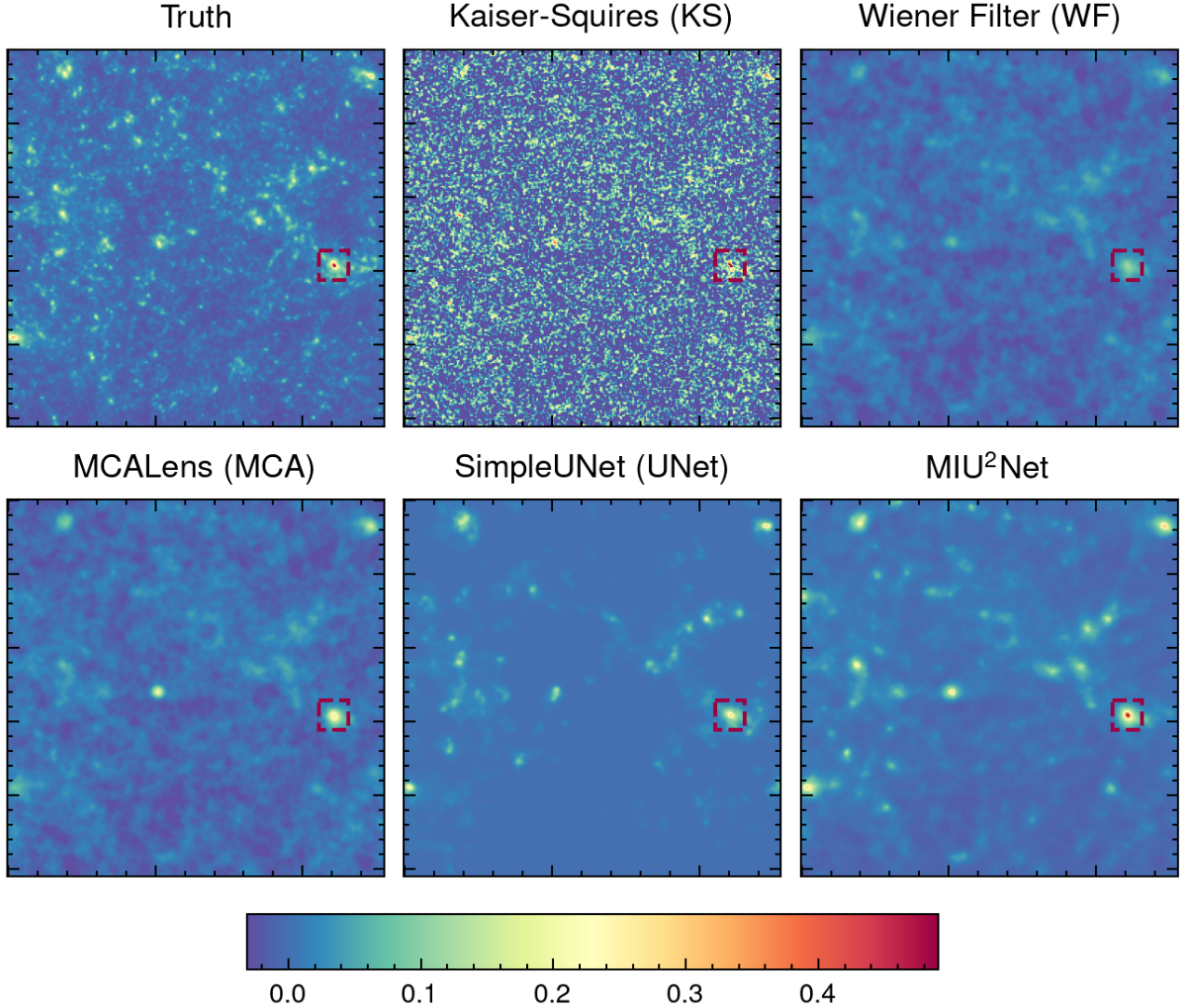


Fig. 1 Visual comparison between Truth, our method (MIU²Net), and established methods including Kaiser-Squires (KS), Wiener filtering (WF), MCALens (MCA), and SimpleUNet (UNet, based on DeepMass). Each panel covers a 1.75×1.75 deg² Euclidean patch of sky. The shear maps used for reconstruction have shape noise corresponding to galaxy number density $n_g = 20$ arcmin⁻². We visualize in detail the scarlet dashed square region in each panel in Fig. 4.

where $\mathcal{D}(\boldsymbol{\theta}) = -1/(\theta_1 - i\theta_2)^2$. This equation can be discretized into a linear model using matrix notation

$$\boldsymbol{\gamma} = \mathbf{A}\boldsymbol{\kappa}, \quad (6)$$

where $\boldsymbol{\gamma}$ and $\boldsymbol{\kappa}$ are vector quantities for shear and convergence sampled on an image grid. Throughout the paper, we assume that the image patch size is small enough for sky geometry to be Euclidean.

In the weak lensing regime, the source galaxies are much smaller than the angular scale where lensing properties vary. This allows us to use Born approximation and write out the amplification matrix \mathcal{A} , a Jacobian that describes the lensing transformation from the source plane to

the image plane

$$\mathcal{A}(\boldsymbol{\theta}) = \begin{pmatrix} 1 - \kappa - \gamma_1 & -\gamma_2 \\ -\gamma_2 & 1 - \kappa + \gamma_1 \end{pmatrix}. \quad (7)$$

Rewriting the amplification matrix and factoring out $(1 - \kappa)$, we have

$$\mathcal{A}(\boldsymbol{\theta}) = (1 - \kappa) \begin{pmatrix} 1 - g_1 & -g_2 \\ -g_2 & 1 + g_1 \end{pmatrix}, \quad g_{1,2} = \frac{\gamma_{1,2}}{1 - \kappa}, \quad (8)$$

where $g = g_1 + ig_2$ is the reduced shear field and is a direct observable. In practice, $\boldsymbol{\gamma}, \boldsymbol{\kappa} \ll 1$ for most weak lensing regions, so that the reduced shear and the true shear are approximately the same, or $g \simeq \boldsymbol{\gamma}$. This allows us to extend the linear relation in (6) for reduced shear. However,

for regions near convergence peaks, κ is not negligible at small angular scales (White 2005; Shapiro 2009), creating a significant discrepancy between shear and reduced shear. It is therefore preferable to reconstruct κ from the reduced shear field \mathbf{g} . For fair comparison, we use the shear field instead of the reduced shear field for all reconstruction methods. In practice, our method can easily incorporate reduced shear by augmenting the training set via (8).

2.2 Shape Noise

Weak lensing information is only sampled at discrete locations where galaxy ellipticities are measured. However, galaxies are not intrinsically circular, so the observed ellipticity is made up of both the galaxy's intrinsic ellipticity and the distortion from weak lensing. This results in a “shape noise” order of magnitudes larger than the weak lensing signal. As shown by van Waerbeke (2000), the observed shear γ_{obs} can be modelled as true shear plus an additive shape noise ϵ , or

$$\gamma_{\text{obs}} \approx \mathbf{g} + \epsilon \approx \boldsymbol{\gamma} + \boldsymbol{\epsilon}. \quad (9)$$

In matrix notation, we write the observed shear as

$$\boldsymbol{\gamma}_{\text{obs}} = \boldsymbol{\gamma} + \mathbf{n} = \mathbf{A}\boldsymbol{\kappa} + \mathbf{n}, \quad (10)$$

where \mathbf{n} is a discrete Gaussian random field with zero mean and variance

$$\sigma_n^2 = \frac{\sigma_\epsilon^2}{2} \frac{1}{\theta_s^2 n_g}, \quad (11)$$

where σ_ϵ is the root-mean-square (RMS) amplitude of the galaxy intrinsic ellipticity distribution, θ_s is the pixel side length in arcmin, and n_g is the galaxy number density per pixel. Throughout the paper, we adopt $\sigma_\epsilon = 0.4$ and galaxy number density of 20 arcmin^{-2} , which are conservative values for next-generation ground- and space-based surveys (Mandelbaum et al. 2018). We can then draw a noise realization \mathbf{n} with the same shape as $\boldsymbol{\gamma}$ and model shape noise by simple matrix addition. For an impression of scale, we have the RMS amplitude of noise about 19 times larger than that of the signal.

2.3 Mass-Sheet Degeneracy

A fundamental limit of weak lensing mass mapping is the mass-sheet degeneracy. (For a detailed discussion, please refer to Falco et al. 1985 in the strong lensing regime, and Schneider & Seitz 1995; Bradač et al. 2004 for weak lensing.) Consider the transformation of the lensing potential

$$\psi(\boldsymbol{\theta}) \rightarrow \psi_\lambda(\boldsymbol{\theta}) = \frac{1 - \lambda}{2} |\boldsymbol{\theta}|^2 + \lambda \psi(\boldsymbol{\theta}), \quad (12)$$

so that we satisfy the Poisson equation (2). λ here is an arbitrary constant. It then follows that the Jacobian in (7) behaves as $\mathcal{A}_\lambda(\boldsymbol{\theta}) = \lambda \mathcal{A}(\boldsymbol{\theta})$, and the convergence as

$$\kappa(\boldsymbol{\theta}) \rightarrow \kappa_\lambda(\boldsymbol{\theta}) = \lambda \kappa(\boldsymbol{\theta}) + (1 - \lambda). \quad (13)$$

The first term is a linear rescaling of the “true” convergence field $\kappa(\boldsymbol{\theta})$, and the second term corresponds to the addition of a homogeneous surface mass density $\kappa_0 = 1 - \lambda$. The convergence κ field can thus only be determined up to this degeneracy transformation. The mass-sheet degeneracy fundamentally limits weak lensing applications, because the reconstructed convergence field can only probe the *fluctuations* of projected matter density on top of an unknown mean, instead of the *absolute* projected matter density. This degeneracy cannot be lifted using ellipticities of background sources alone (Seitz & Schneider 1997) and fundamentally limits weak lensing in determining the absolute mass distribution.

2.4 Missing Data

Another strong observational limitation is missing data. This is due to complex survey geometry, masking of bright stars, image reduction masks, defects in CCD sensors, etc. The observed shear tensor is therefore further modified by a binary mask operator specific to each image. Missing data is usually filled with 0, or, more sophisticatedly, filled by inpainting methods using Discrete Cosine Transform (DCT) (Pires et al. 2009, 2020). We approach the missing data problem in a similar vein as DCT, guiding deep learning to learn a frequency domain energy distribution inside the masked area.

3 MASS INVERSION METHODS

In this section, we briefly introduce some of the standard methods of weak lensing mass inversion, then go on to illustrate the deep learning approach. We will then build on the standard deep learning framework and introduce MIU²Net in the next section.

3.1 Kaiser-Squires (KS)

Kaiser & Squires (1993) have shown that we can reconstruct the convergence field in the Fourier domain. Consider Eq. (5) where the complex shear $\boldsymbol{\gamma}$ is a convolution on κ with the kernel \mathcal{D} . We know that a convolution in the spatial domain is equivalent to an element-wise multiplication in the Fourier domain, therefore

$$\tilde{\boldsymbol{\gamma}}(\mathbf{k}) = \pi^{-1} \tilde{\mathcal{D}}(\mathbf{k}) \tilde{\kappa}(\mathbf{k}), \quad \mathbf{k} \neq 0, \quad (14)$$

where \mathbf{k} is the wavevector, and the tildes denote Fourier transforms. The Fourier transform of $\mathcal{D}(\theta)$ is

$$\tilde{\mathcal{D}}(\mathbf{k}) = \pi \frac{(k_1^2 - k_2^2 + 2ik_1k_2)}{|\mathbf{k}|^2}, \quad (15)$$

which satisfies $\tilde{\mathcal{D}}(\mathbf{k})\tilde{\mathcal{D}}^*(\mathbf{k}) = \pi^2$. Inverting Eq. (14) then yields

$$\tilde{\kappa}(\mathbf{k}) = \pi^{-1}\tilde{\gamma}(\mathbf{k})\tilde{\mathcal{D}}^*(\mathbf{k}), \quad \mathbf{k} \neq 0. \quad (16)$$

Transforming back to the spatial domain, we obtain the mass inversion

$$\kappa(\theta) - \kappa_0 = \frac{1}{\pi} \int_{\mathbb{R}^2} d^2\theta' \mathcal{D}^*(\theta - \theta') \gamma(\theta'). \quad (17)$$

The arbitrary constant κ_0 arises because the inversion is undefined when $\mathbf{k} = 0$, which is the effect of the mass-sheet degeneracy. In practice, it is often assumed that the mean convergence vanishes for a large enough field, i.e., $\kappa_0 = 0$. In addition, the standard KS deconvolution does not take into account noise, reduced shear, or masked data, and can therefore introduce errors in the reconstruction.

3.2 Wiener Filtering (WF)

Another widely used mass inversion method is Wiener filtering (Lahav et al. 1994; Zaroubi et al. 1995). The Wiener filter is the linear minimum-variance solution for the general recovery problem in Eq. (10), assuming a Gaussian prior. If the noise is uncorrelated, Wiener filtering reconstructs convergence map $\hat{\kappa}_{\mathbf{W}}$ by the linear relation

$$\hat{\kappa}_{\mathbf{W}} = \mathbf{W}\gamma_{\text{obs}}, \quad (18)$$

where \mathbf{W} is the Wiener filter

$$\mathbf{W} = (\mathbf{A}\Sigma_s\mathbf{A}^\dagger + \Sigma_n)^{-1} \mathbf{A}^\dagger \Sigma_s. \quad (19)$$

Here, $\Sigma_s = \langle \kappa\kappa^\dagger \rangle$ and $\Sigma_n = \langle \mathbf{n}\mathbf{n}^\dagger \rangle$ are the covariance matrices for the convergence signal and noise, respectively. \mathbf{A} is the linear model matrix in Eq. (6), and \mathbf{A}^\dagger is its conjugate transpose. From the Bayesian perspective, WF assumes a zero-mean Gaussian prior in the form

$$p(\kappa|\Sigma_s) = |2\pi\Sigma_s|^{-\frac{1}{2}} \exp\left[-\frac{1}{2}\kappa^\dagger \Sigma_s \kappa\right], \quad (20)$$

and the reconstruction result $\hat{\kappa}_{\mathbf{W}}$ is the *maximum a posteriori* (MAP) solution of $p(\kappa|\gamma)$, assuming that both signal and noise are gaussian random fields. If $\Sigma_n = 0$, WF reduces to KS deconvolution (Simon et al. 2009). The Gaussian prior is physically motivated on large scales, but it is less appropriate for smaller scales where structure formation is non-linear. Like KS, WF assumes a zero-mean convergence during implementation.

Jeffrey et al. (2021) point out that the MAP solution $\hat{\kappa}$ that maximizes $p(\kappa|\gamma)$ is not necessarily the MAP solution for the transformed probability $p(f(\kappa)|\gamma)$. WF is

thus not ideal for inferring cosmology, because a statistic on the Wiener posterior is no longer the most probable statistic. To estimate a given statistic μ , we can instead sample from the joint posterior $p(\kappa, \mu|\gamma)$. Several works have shown that a joint estimate of the convergence map and its power spectrum is possible (Wandelt et al. 2004; Alsing et al. 2017).

3.3 Deep Learning

The burst of deep learning in recent years has brought paradigm shifts to many academic fields. Compared to task-specific solvers, a self-learned gigantic parametric model seems to perform much better on ill-posed inverse problems. The model is often intentionally vague and non-transparent, yet it generalizes very well and handles unseen data with surprising sophistication. In the language of deep learning, we can approach the inverse problem in Eq. (10) as a supervised image-to-image translation problem with these general steps:

1. Prepare a large “clean” dataset on the order of thousands or even millions of images. For weak lensing mass inversion, this means obtaining many shear and convergence realization pairs from simulations. This paired dataset will be the source from which the model learns a transformation.
2. Degrade the images-to-be-learned by noise realizations, random data masks, reduced shear, etc., so that the shear images resemble real observations.
3. Construct a parametric model to learn the transformation from noisy (reduced) shear to true convergence. The model represents a Universal Function Approximator, where it essentially learns a non-linear mapping \mathcal{F} between its inputs and outputs. The model is often called a “network” because it consists of billions of interconnected neurons, much like the biological neural networks in our brains.
4. Define a loss function \mathcal{L} that tells the network how bad the reconstruction is, and which way it should move to improve the reconstruction. Iterating through the dataset, the network nudges its billions of parameters to minimize this loss function. This is what we mean by “learning” in deep learning.
5. Test the network using data pairs not revealed during training. If the network performs well on unseen data, it can generalize to observational data with similar degradation.

For translation-invariant data, the network in step. (iii) is often a Convolutional Neural Network (CNN) that learns to optimize layers of convolution kernels (LeCun et al. 1989). CNN is effectively a sparsely-connected neural network, where each neuron is only responsive to a restricted

field of neurons in the previous layer. This field is often called the CNN’s *receptive field*. For a CNN with similar kernel sizes in each layer, the receptive field is small because the network is only sensitive to the scale of features that can be amplified by convolution kernels of a particular size. Efforts to enlarge the receptive field led to the development of the UNet architecture (Ronneberger et al. 2015), which uses a *contracting path* and an *expansive path* to learn long-range spatial dependencies. The contracting path encodes the inputs by downsampling after each convolution, reducing spatial dimensions and iterating through different receptive field sizes. The expansive path then decodes the data by up-convolutions, while using skip connections to receive information from the contracting path. The U-shaped architecture is sensitive to different scales of features, and is thus very useful in image segmentation, classification, and translation tasks.

In the context of Dark Energy Survey (DES) Scientific Validation (SV), Jeffrey et al. designed the first UNet for weak lensing mass inversion (DeepMass; Jeffrey et al. 2020). The input shear data is first passed through the Wiener filter in Eq. (18), then fed into UNet for non-linear refinement on the Wiener posterior to obtain the deep-learning reconstruction

$$\hat{\kappa}_{\text{UNet}} = \mathcal{F}(\mathbf{W}\gamma), \quad (21)$$

where \mathcal{F} is learned by the network. The use of Wiener filtering compresses input shear to real space and reduces memory consumption, but in turn necessitates an input power spectrum in the form of a signal covariance matrix Σ_s . The loss function in step. (iv) is the mean square error (MSE) loss, or the squared l_2 norm

$$\mathcal{L}(\hat{\kappa}_{\text{UNet}}, \kappa) = \text{MSE} = \mathbb{E} (\|\kappa - \hat{\kappa}_{\text{UNet}}\|_2^2), \quad (22)$$

which is the standard loss function in deep learning.

4 MIU²NET

We propose Mass-Inversion-U²Net (MIU²Net), a versatile deep learning framework for weak lensing mass inversion. We adapt a nested UNet architecture (U²-Net; Qin et al. 2020) for image translation tasks, and construct a new loss function to jointly optimize MSE and the frequency domain energy distribution. We introduce our simulation, network architecture and loss function in this section. Hyperparameters and technical details for training can be found in Appendix A.

4.1 Training Data

Our training data is obtained from ray-tracing dark matter simulations. In order to cover the space between $0 < z \leq 1$, we concatenate 8 pseudo-independent cubic boxes

where each box has side length $320 h^{-1} \text{Mpc}$ and contains 640^3 dark matter particles, each with mass $0.97 \times 10^{10} h^{-1} \text{M}_\odot$. The 8 boxes share the same initial conditions, but are at different redshifts and are made pseudo-independent via translations and rotations. We have 4 sets of boxes with different initial conditions (where each set contains 8 boxes sharing the same initial conditions.) The cosmological constants used in the simulations are $\sigma_8 = 0.82$, $\Omega_m = 0.28$, $\Omega_\Lambda = 0.72$, $\Omega_b = 0.046$, $h = 0.7$, and $n_s = 0.96$.

In order to construct lensing systems, we divide each box into 5 segments according to comoving distance along the line-of-sight. All particles in the segments are then projected onto 2D slices acting as lens planes. We have a total of 37 lens planes between $0 < z \leq 1$ (the last box is not fully used). We then utilize multi-plane ray-tracing (Hilbert et al. 2009) to obtain 6000 pairs of shear maps γ and convergence maps κ . The map sizes are $3.5 \times 3.5 \text{ deg}^2$ pixelated into 1024×1024 pixels.

We then prepare our training data for machine learning by dividing the data into 5000 pairs of training data and 1000 pairs of validation data. If we need to utilize reduced shear, we can easily compute a third set of reduced shear maps by equation (8) from clean $\gamma - \kappa$ pairs. For fair comparisons, we omit this step and instead train our network on $\gamma - \kappa$ pairs. Then, we generate a shape noise realization corresponding to 20 galaxies arcmin^{-2} and add it to shear maps according to equation (11). In principle, MIU²Net sees a new training pair every time because the random shape noise realization completely dominates the shear field. After adding shape noise, we randomly crop each map to 512×512 pixels, before downsampling them to 256×256 to reduce memory consumption. To prevent over-fitting, we augment our data by random horizontal flips, vertical flips, and 90° rotations. In this way, we obtain 320000 independent pairs of training data and many more pairs with overlapped regions. To mimic bright star masks in observational settings, we generate a random bright star mask and apply it to the noisy reduced shear map every time MIU²Net sees a training sample. The bright star masks consist of circular radii following a power law distribution and randomly cover 0 – 25% of the pixel areas for every realization. By randomising mask percentage during training, the network can be versatile against different mask levels, and can reliably reconstruct convergence maps without retraining.

4.2 Architecture

MIU²Net is based on U²-Net originally designed for salient object detection (Qin et al. 2020). U²-Net is a nested UNet structure that greatly increases network depth with-

out significantly increasing the computation cost. It has a large encoder-decoder U-structure, where each stage is a well-configured UNet with residual connections. Each decoder stage predicts a saliency probability map $S_{\text{side}}^{(m)}$, and the final prediction is a weighted average of all $S_{\text{side}}^{(m)}$ where the weights are learned via 1x1 convolution. In this way, U²-Net can efficiently fuse information at all scales. The detailed design of U²-Net is not the focus of this paper, and we encourage the reader to refer to the original paper and PyTorch implementation here.

The original saliency probability maps fall between 0 and 1 because they denote the probability of each pixel belonging to the salient object. MIU²Net removes the sigmoid function at the end of each decoder stage, so that the map intensities are no longer bounded and can correspond to true convergence maps. Fig. 2 shows the architecture of MIU²Net in detail. During training, MIU²Net takes the degraded complex reduced shear g^n as a two-channel input and outputs the true convergence map, learning a non-linear mapping

$$\hat{\kappa}_{\text{MIU}^2\text{Net}} = \mathcal{F}(g^n). \quad (23)$$

Further extensions to MIU²Net are simple. We can fuse information from the projected halo distribution, for example, by simply appending the halo distribution map as a third channel to the input. The network will adjust its parameters to learn an optimal fusion.

4.3 Loss Function

The original U²-Net has its loss function as a standard binary cross-entropy, because each pixel in the saliency probability maps is essentially a binary classification problem. To adapt it to our image translation task, we use a pixel-wise MSE loss as used by (Jeffrey et al. 2020). However, MSE-based networks are inclined to make conservative, blurry predictions averaged over all possible solutions weighted by their posterior probabilities, instead of learning the actual image manifold (Blau & Michaeli 2018; Elad et al. 2023). This would make the minimum MSE (MMSE) result unrepresentative of the image distribution and influence global statistics. To obtain summary statistics from the MMSE solution, we encounter a similar problem as WF because the pixel values that form the optimized reconstruction $\hat{\kappa}$ do not optimize its statistics $f(\hat{\kappa})$.

We approach this problem by adding a radial-averaged power spectrum (RAPS) term in the loss function \mathcal{L} , so that we jointly optimize MSE and the frequency-domain reconstruction quality. The deep learning convergence map can then be used for inference and summary statistics. In addition, tuning the weights for different loss terms designates their relative importance and balances between optimal mean convergence and optimal summary statistic. It

must be stressed, however, that a joint estimation is never the optimal estimation for each. One should tune their relative importance with respect to each application.

We denote the six decoder-stage maps as $\hat{\kappa}_{\text{side}}^{(m)}$ and the final output map as $\hat{\kappa}_{\text{fuse}}$. The loss function is computed between the true convergence map κ and each of the decoder-stage maps, as well as between κ and the final output map. During training, the loss function \mathcal{L} is the total loss of all seven maps, or

$$\mathcal{L} = w_{\text{fuse}} l_{\text{fuse}} + \sum_{m=1}^6 w_{\text{side}}^{(m)} l_{\text{side}}^{(m)}, \quad (24)$$

where l_{fuse} is the loss between κ and $\hat{\kappa}_{\text{fuse}}$, and $l_{\text{side}}^{(m)}$ is the loss between κ and each of $\hat{\kappa}_{\text{side}}^{(m)}$. w_{fuse} and $w_{\text{side}}^{(m)}$ are weights for each loss term. We choose w_{fuse} and all $w_{\text{side}}^{(m)}$ to be 1. For each pair of true κ and reconstructed $\hat{\kappa}$ where we compute a loss term l , we have

$$l = \alpha l_{\text{MSE}} + \beta l_{\text{RAPS}}, \quad (25)$$

where l_{MSE} and l_{RAPS} are the MSE loss term and the RAPS loss term, respectively. α and β determine their relative importance.

The MSE loss term l_{MSE} is the standard MSE defined in Eq. (22). We rewrite it into a clearer form:

$$l_{\text{MSE}}(\kappa, \hat{\kappa}) = \frac{1}{H \times W} \sum_{(i,j)}^{(H,W)} (\kappa_{i,j} - \hat{\kappa}_{i,j})^2, \quad (26)$$

where (H, W) is the height and width of the convergence maps, here taken to be (256, 256).

The RAPS loss term l_{RAPS} quantifies reconstruction quality in the frequency domain. For each pair of κ and $\hat{\kappa}$, we take their Discrete Fourier Transforms and compute their respective power spectra $P_{\kappa}(u, v)$ and $P_{\hat{\kappa}}(u, v)$. We define the radial-average power spectrum as

$$\bar{P}_{\kappa}(r) = \frac{1}{N(r)} \sum_r P_{\kappa}(u, v), \quad (27)$$

where the summation is performed over all Fourier-space coordinates at a distance r from the DC component, i.e., over all (u, v) pairs that satisfy $r - 1 \leq \sqrt{u^2 + v^2} < r$. $N(r)$ denotes the number of (u, v) pairs within this annulus. In practice, it is impossible to reconstruct the high-frequency fluctuations under realistic noise, so we limit RAPS to low frequencies (central regions in Fourier space) and only consider r values up to r_{max} . We choose $r_{\text{max}} = 16.0$ in this paper. The RAPS loss is then defined as the Mean Absolute Error (MAE) between central regions of true and predicted radial-average power spectra, or

$$l_{\text{RAPS}}(\kappa, \hat{\kappa}) = \frac{1}{r_{\text{max}}} \sum_{r=0}^{r_{\text{max}}} |\bar{P}_{\kappa}(r) - \bar{P}_{\hat{\kappa}}(r)|. \quad (28)$$

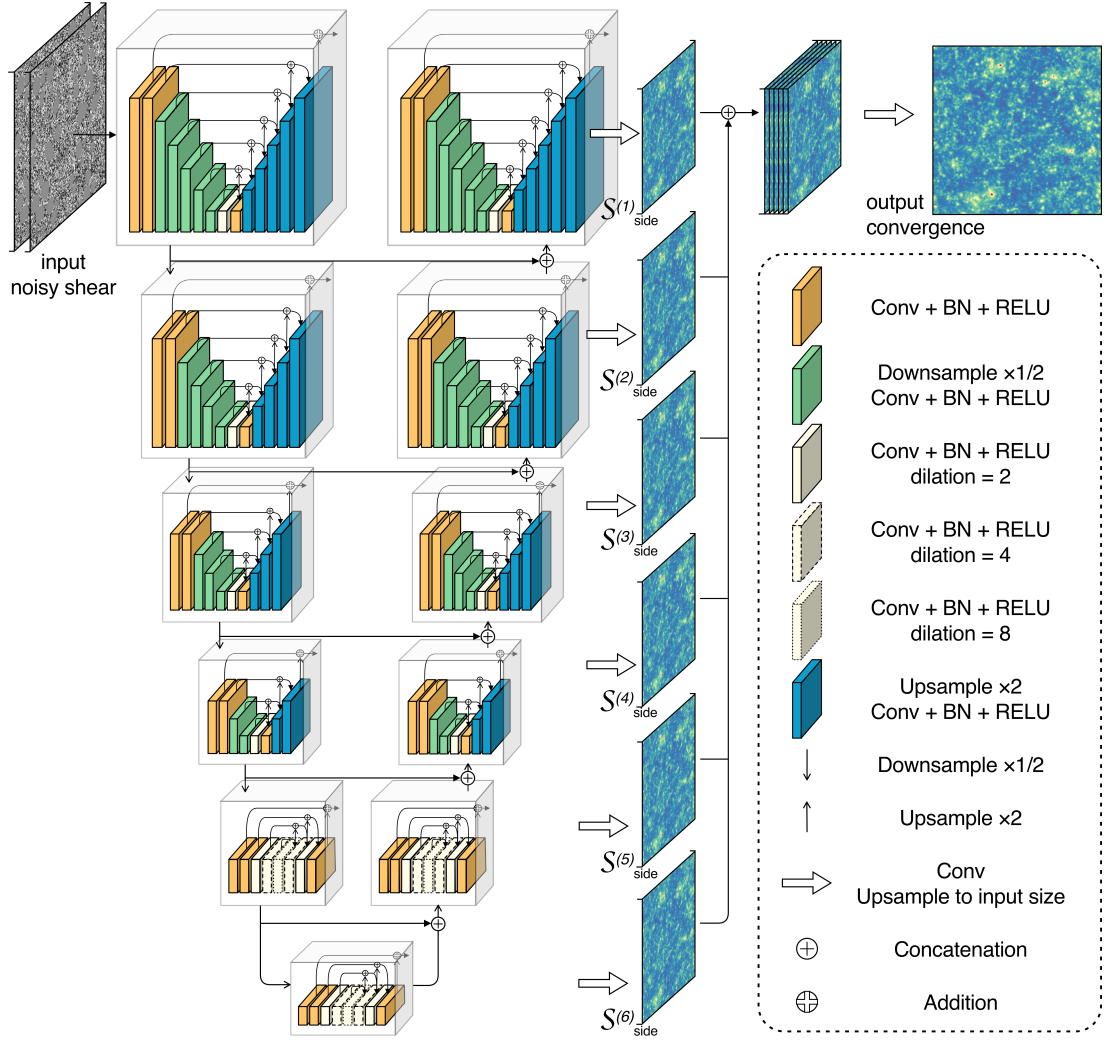


Fig. 2 MIU²Net structure adapted from U²-Net. Figure is drawn based on Fig. 5 in Qin et al. (2020).

5 RESULTS

In this section, we compare our convergence maps to those obtained by established methods, including unsupervised methods such as Kaiser-Squires (KS), Wiener filtering (WF), MCALens (MCA) (Starck et al. 2021), and supervised deep learning methods such as DeepMass (UNet) (Jeffrey et al. 2020). For easier comparison with established methods, we first test MIU²Net with shear maps polluted only by shape noise, i.e., using the degraded shear field γ^n instead of the reduced shear g^n , and adding no data masks. The results are outlined in Sect. 5.1–5.5. We then demonstrate MIU²Net’s generalization across cosmologies in Sect. 5.6, and its ability to deal with data masks in the full training in Sect. 5.7. In all test cases, we use the same trained model without further retraining or fine-tuning.

For DeepMass reconstructions, because the original implementation is designed for DES SV mass inversion,

we replicate the authors’ network structure and retrain the model on our simulation for 512 epochs (network converges at about 200 epochs). Because our replication is not the same as the official DeepMass, we change the name to “SimpleUNet” or the shorthand “UNet”. For MCALens, we use $\lambda = 5$ and **InpWiener** for inpainting, as illustrated in Starck et al. (2021). For both Wiener filtering and MCALens, we input the correct signal power spectrum into the algorithms. There are also many variants of these established methods (e.g. inpainting using different priors, as in Pires et al. (2009); Lanusse et al. (2016); Pires et al. (2020); Starck et al. (2021), and iterative E-mode convergence estimation, as in Seitz & Schneider (1995); Jullo et al. (2014)). For future studies, a thorough comparison is desired to characterize MIU²Net relative to each of the traditional variants.

5.1 Perceptual Quality

Fig. 1 shows a visual comparison between MIU²Net, KS, WF, MCA, and UNet reconstructions. A few things are immediately noticeable:

1. MIU²Net has the best perceptual quality and most accurately represents the data distribution. It has superior reconstruction quality from large-scale, filament-like structures to well-defined, non-Gaussian peaks.
2. Compared to KS reconstruction, MIU²Net is highly effective in suppressing noise.
3. MIU²Net reconstruction is very similar to WF in terms of large-scale diffusive structures. Although we do not feed WF into MIU²Net in any way, MIU²Net seems to have learned the WF result.
4. MIU²Net reconstructions have well-defined local peaks. The peak centroids are close to the true centroids and can potentially be used to locate hidden dark matter halos.

Part of the good perceptual quality arises from MIU²Net’s ability to recover the true dynamic range of convergence maps. Fig. 3 shows the dynamic range recovery for MIU²Net, KS, WF, MCA, and UNet. MIU²Net significantly outperforms other methods in recovering the lower and upper bounds of individual convergence maps. Importantly, the upper bound $\max(\kappa)$ of a given convergence map corresponds to the pixel with the most intensity, and therefore with the most concentrated projected matter density in a region. Accurate recovery of the position and amplitude of $\max(\kappa)$ is crucial for finding hidden mass concentrations that are absent in the electromagnetic space.

We also visualize an example mass density peak to show MIU²Net’s reconstruction of peak centroid and amplitude. Fig. 4 shows a mass density peak in the true convergence map, as well as the same regions in the reconstructions by MIU²Net, KS, WF, MCA, and UNet. Although KS has a decent reconstruction of the central intensity, it is very noisy and less sensitive for lower convergence values. Compared to WF, MCA, and UNet, the MIU²Net peak is much more prominent; its amplitude is also much closer to the true amplitude. MIU²Net also has optimal peak recovery based on Full Width at Half Maximum (FWHM) measures. However, the MIU²Net peak profile is still relatively smooth, and it fails to reproduce the highly non-Gaussian profile of a true convergence peak.

5.2 On the Mass-Sheet Degeneracy

As shown in Eq. (13), mass-sheet degeneracy prohibits us from recovering the mean convergence from the ellipticity field. MIU²Net, however, appears to be capable of inferring the mean convergence using only the shear field.

This may be primarily due to the prior of the training set used. As shown in Fig. 5, instead of assuming mean convergence to vanish, MIU²Net recovers the mean with some scatter. The slope of the best-fit line is less than 1, which is expected because MSE-based loss functions are inclined to produce conservative, middle-ranged reconstructions. Both MIU²Net and UNet exhibit a positive slope, but MIU²Net recovers the mean convergence better and has a negligible overall bias. We thus introduce the simple correction factor $\mu_{\text{ms}} = 1.672$, so that the corrected MIU²Net statistics $\mu_{\text{ms}}\langle\hat{\kappa}\rangle$ matches the ideal recovery, as shown in the middle panel of Fig. 5. Interestingly, although we only introduce a scaling factor, it is robust under a significantly different cosmology (right panel in Fig. 5) and 20% masked conditions (see Fig. B.4). The second cosmology is outlined in detail in Sect. 5.6. This suggests that our empirical correction factor obtained from a single, fiducial cosmology generalizes across cosmologies for reconstructing dark matter environment. Many methods have been proposed to lift the mass-sheet degeneracy (Seitz & Schneider 1997; Bradač et al. 2004; Rexroth et al. 2016; Cremonese et al. 2021); with additional data such as redshift distribution, flexion fields, and gravitational wave inferences, MIU²Net and deep learning estimators offer the prospect of breaking the mass-sheet degeneracy and probing the absolute mass density distribution.

5.3 Convergence Distribution

The distribution of convergence values follows a log-normal distribution with an extended tail (Jain et al. 2000; Hilbert et al. 2011; Clerkin et al. 2017). Fig. 6 shows the convergence distribution in terms of Kernel Density Estimation (KDE) for truth and all reconstruction methods. In the left panel, we show that none of the methods recovers the true distribution well, but MIU²Net has a log-normal shape similar to that of the truth. We then transform each reconstruction method by the normalization $\kappa \rightarrow (\kappa - \langle\kappa\rangle)/\sigma_\kappa$, where $\langle\kappa\rangle$ and σ_κ are the mean and standard deviation of all constituent pixels in all maps reconstructed by that method. The distribution for normalized convergence values for each method is shown in Fig. 6, middle panel. The normalized MIU²Net properly recovers the true distribution, whereas KS, WF, and MCA are symmetric and cannot recover the log-normal curve. UNet has a large portion of pixels around $\kappa = 0$ and does not follow the true distribution as well. The right panel zooms in on the high-end extended tail largely resembling convergence peaks. We show that KS and WF fall off rapidly, yet MIU²Net closely follows the extended tail to very high convergence values until the true distribution itself starts to exhibit high variance. MIU²Net’s slight

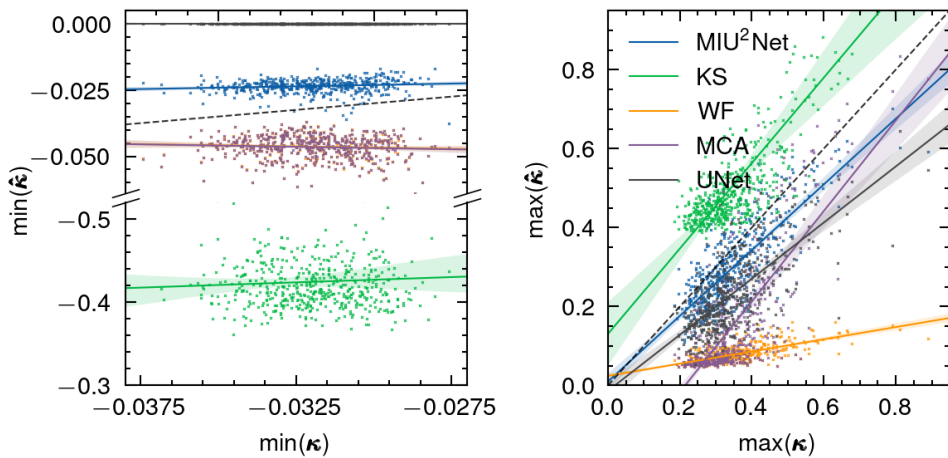


Fig. 3 Dynamic range for each of the 500 convergence reconstructions from MIU²Net, KS, WF, MCA, and UNet. *Left panel*: minimum predicted convergence value $\min(\hat{\kappa})$ against minimum true convergence value $\min(\kappa)$ for each reconstruction. We also plot the best-fit lines, and the shadings indicate the 95% confidence intervals for each method. The coloured dots follow the same labelling scheme as in the right panel. The black dashed line is the $y = x$ line denoting ideal reconstruction. Note that MIU²Net can best recover the lower bound, but it systematically overestimates it when $\min(\kappa)$ is low. KS reconstructions cluster around the lower region far away from truth, because KS is symmetric around 0 and does not provide a good estimate for the lower bound. *Right panel*: scatter plot and best-fit lines for maximum values for each true-prediction pair. The shadings indicate the 95% confidence intervals for each method. Again, the black dashed line is the $y = x$ line tracing the ideal reconstruction. It is clear that MIU²Net has a slope closest to the ideal and can reliably predict the upper bound of individual convergence maps. Nevertheless, MIU²Net systematically underestimates the upper bound. This is expected because an MSE-based estimator is inclined to make blurry, middle-range predictions that smooth out intense spikes. Compared to UNet, which is also an MSE-based estimator, MIU²Net more reliably recovers the maximum amplitude. As seen by the larger slope, MIU²Net is more inclined to make bold, salient predictions than UNet for larger maximum peaks.

overestimation for the extended tail can be attributed to its imperfect recovery of non-Gaussian peak profiles, as seen qualitatively in Fig. 4. Because a MIU²Net peak does not rise as steeply as a true peak, extra intensity around the peak centroid may lead to overestimated probability density at middle and high convergence values.

5.4 Power Spectrum

One of the most important aspects of weak lensing studies to this date has been the measurement of two-point statistics (Hildebrandt et al. 2017; Troxel et al. 2018; Hikage et al. 2019; Hamana et al. 2020). For a zero-mean Gaussian density field, two-point statistics like the power spectrum or two-point correlation functions can completely characterize the data. However, systematic studies on popular methods such as KS, WF, null B-mode prior, and sparsity prior (Glimpse; Lanusse et al. 2016) have shown that none of these methods can reliably reconstruct the power spectrum (Jeffrey et al. 2021). Importantly, these methods differ in their priors used, but all are MAP estimators for the most probable map $\hat{\kappa}$ instead of the most probable summary statistic. Current deep learning methods, on the other hand,

often focus on pixel-wise, MMSE-only reconstruction that does not translate well to the frequency domain. It has also been shown that a conditional generative adversarial network incorporating a learned loss function still cannot accurately recover the power spectrum under a more lenient noise per pixel than what is used in this paper (Shirasaki et al. 2019).

In Sect. 4.3, we have designed a combined loss function that enables MIU²Net to jointly estimate a pixel-wise reconstruction and the frequency domain power distribution. We demonstrate in Fig. 7 that MIU²Net can reconstruct the convergence power spectrum with 4% uncertainties in the multipole range $0 < l \lesssim 500$, far exceeding existing reconstruction methods at all scales. Compared to WF and MCA with optimal input signal power spectra, MIU²Net achieves 1060% and 930% improvements in reconstruction quality at $l \simeq 500$. Changing the high-frequency cutoff r_{\max} in Eq. (28) changes the highest multipole number l considered in the loss function, so MIU²Net can potentially reach even smaller angular scales with careful tuning. At the lowest frequency bin where recovering the DC component is subjected to the mass-sheet degeneracy, MIU²Net has -20.2% reconstruction error,

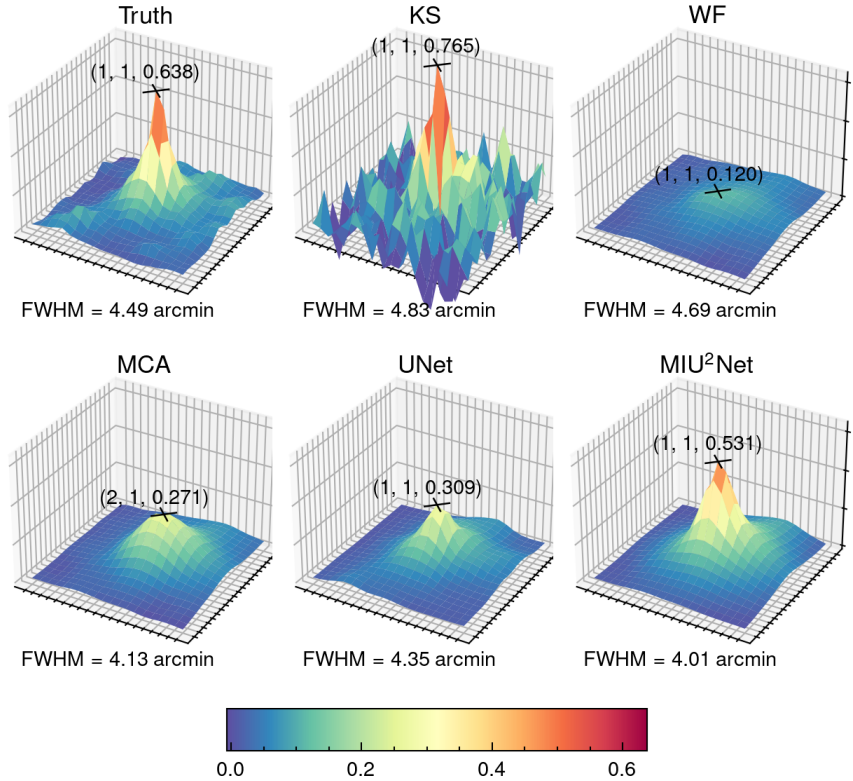


Fig. 4 Centroid and amplitude recovery from MIU²Net, KS, WF, MCA, and UNet for an individual convergence peak. The plotted regions have dimensions $8.2 \times 8.2 \text{ arcmin}^2$ and correspond to the scarlet dashed square regions in Fig. 1. The crosses indicate the highest peak in each of the recovered regions. The coordinates above the crosses are in the form $(\Delta x, \Delta y, \kappa_{\text{peak}})$, where Δx and Δy are spatial coordinates of the predicted peak relative to that of the true peak, and κ_{peak} is the peak convergence value. The Full Width at Half Maximum (FWHM) for each peak is shown in the bottom left of each panel. MIU²Net best recovers the position, amplitude, and FWHM of the true peak without significant noise. However, MIU²Net fails to recover the highly non-Gaussian profile of the true peak, as the reconstruction still exhibits a relatively smoothed profile and a bell-like shape. Note that although KS recovers the central peak with decent accuracy, this is because the central peak has a large convergence value (0.638). For lower convergence values, noise can easily submerge the reconstructed peak.

whereas KS and WF have -54.4% and -62.5% error in the same frequency bin, respectively.

The effect of intrinsic alignment and other systematic becomes important when we can constrain the power spectrum to within $\pm 4\%$ up to $l \simeq 500$. Intrinsic alignment can introduce several percent of uncertainties in two-point statistics (Joachimi et al. 2013; Pires et al. 2020), but we do not yet have simulations that can model and study intrinsic alignment in detail. Other sources of error such as PSF modelling, photometric redshift, shear estimation, baryonic effects, and data preprocessing should also receive more attention as they start to become more prominent in the error budget. Although the error in power spectrum reconstruction (4%) is yet insufficient for constraining cosmological parameters, regularising our MMSE estimator in the frequency domain can encourage the network to predict the right amount of peaks of different scales, es-

pecially peaks with higher spatial frequencies. Compared to pure MMSE estimators that tend to produce blurry, averaged predictions, MIU²Net can better match the amplitude of large convergence peaks, as well as predict areas of intermediate convergence values from faint shear signals. This can greatly help map the distribution of large-scale structures in the universe, where filaments are usually fainter than local overdensities. Compared to non-MMSE deep learning networks, such as conditional GAN variants with a trained loss function (Shirasaki et al. 2019), frequency-domain regularization may offer more advantage in estimating the convergence power spectrum. Our method can thus open many possibilities, including galaxy evolution studies under different dark matter environments (i.e. filaments, voids, peaks). In the future, improved training datasets with multiple cosmologies can greatly enhance

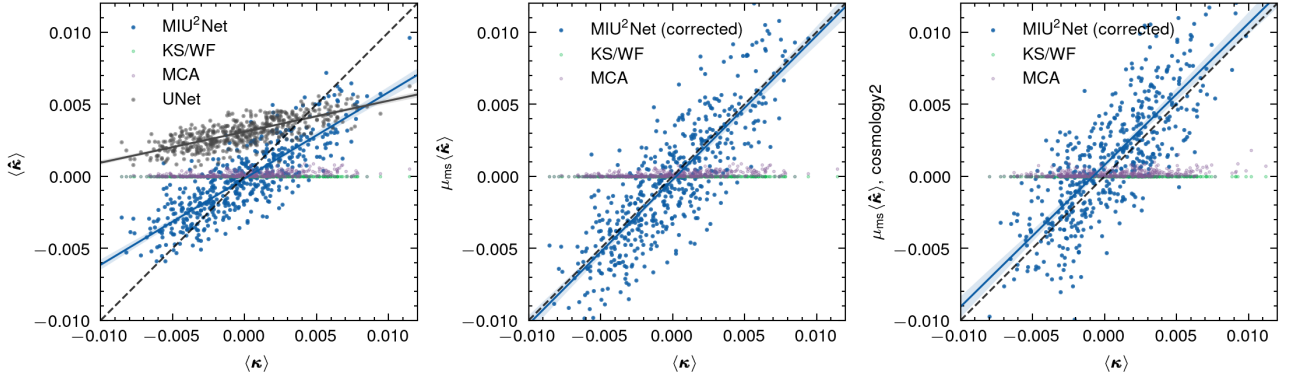


Fig. 5 On the mass-sheet degeneracy. *Left panel*: for 500 reconstructions, we plot the mean $\langle \hat{\kappa} \rangle$ for each of the predicted convergence maps against the mean $\langle \kappa \rangle$ for each of the true convergence maps. The black dashed line is the $y = x$ line denoting the ideal recovery of mean convergence. MIU²Net reconstructions clearly follow a linear relation whose slope is close to the ideal and has a negligible offset. The blue line and shading indicate the best-fit line for MIU²Net and the 95% confidence interval. Both KS and WF assume $\langle \hat{\kappa} \rangle = 0$, so they overlap on the $y = 0$ line. UNet also exhibits a positive slope, suggesting that deep learning MMSE estimators may utilize the prior information in convergence fields better than other methods. *Middle panel*: the same as left panel, except now we plot the corrected MIU²Net reconstructions with $\mu_{\text{ms}} = 1.672$. The value of μ_{ms} is chosen empirically based on the parameters of the best-fit line in the left panel. The best-fit line for corrected MIU²Net closely resembles the ideal linear relationship. *Right panel*: the corrected MIU²Net reconstructions with the same scaling factor $\mu_{\text{ms}} = 1.672$ for reconstructions using the second cosmology. The corrected mean convergence is still very close to the ideal reconstruction despite the change in cosmology.

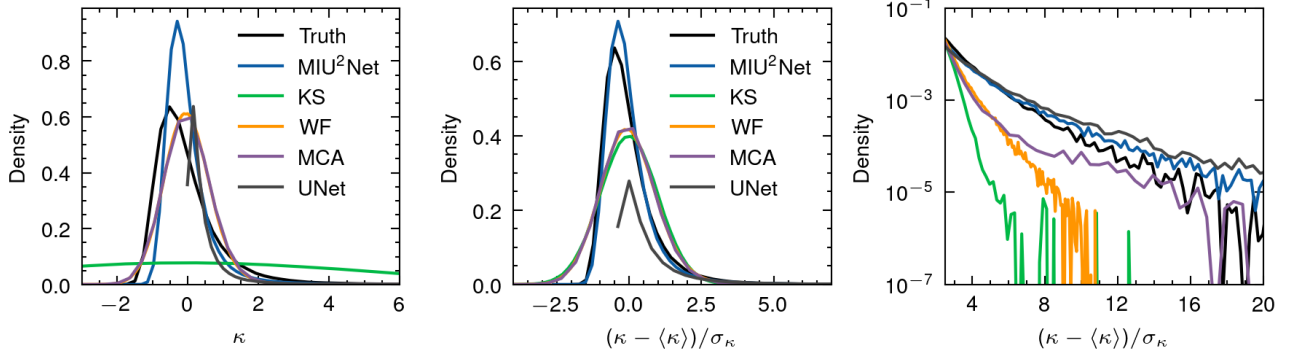


Fig. 6 Convergence probability density distribution for MIU²Net, KS, WF, MCA, and UNet. *Left panel*: Kernel Density Estimation (KDE) for 500 reconstructions. No method appears to recover the true distribution, but the MIU²Net distribution follows a log-normal curve similar to the truth. *Middle panel*: KDE for the same 500 reconstructions normalized by the mean and standard deviation of all constituent pixels. The normalized MIU²Net closely resembles the true distribution, whereas KS, WF, and MCA are symmetric around 0 and do not exhibit any log-normal shape. UNet has a significant amount of pixels around $\kappa = 0$ and does not follow the true distribution. *Right panel*: a zoom-in for the extended high-end tail for normalized distributions. The y -axis is in log scale for better visualization. Note that KS and WF fall off rapidly, whereas MIU²Net recovers the extended tail with slight overestimation at the high end.

our reconstructions and enable MIU²Net to constrain cosmological parameters.

5.5 RMSE

We also evaluate our reconstruction results with Root Mean Square Error (RMSE) under different smoothing conditions. Let

- $\text{Ind} = \{i \mid M[i] = 1\}$ be the indices of the mask,
- M be the binary mask (with the same shape as image),
- $G_\sigma(\cdot)$ be the Gaussian smoothing operator with a smoothing kernel of FWHM σ ,
- $\kappa, \hat{\kappa}$ be the truth and reconstructed convergence maps, respectively.

Then Define

$$\begin{aligned} Z_\sigma &= M \cdot G_\sigma(M \cdot \kappa), \\ Z_\sigma[\text{Ind}] &= Z_\sigma[\text{Ind}] - \text{mean}(Z_\sigma[\text{Ind}]), \\ X_\sigma &= M \cdot G_\sigma(M \cdot \hat{\kappa}), \\ X_\sigma[\text{Ind}] &= X_\sigma[\text{Ind}] - \text{mean}(X_\sigma[\text{Ind}]), \end{aligned}$$

So we have the normalized RMSE

$$\text{RMSE}(\sigma) = \sqrt{\frac{\sum_{\text{Ind}} (Z_\sigma - X_\sigma)^2}{\sum_{\text{Ind}} Z_\sigma^2}}. \quad (29)$$

In this way, we can calculate RMSE without taking into account the mean value of the convergence field and the masked areas. Note that by standard practices KS requires a smoothing on small angular scales, which is itself also a free parameter. Fig. 8 shows that MIU²Net achieves significantly lower RMSE than established methods across all smoothing scales. At larger smoothing scales, MIU²Net is increasingly more accurate than other methods, demonstrating that MIU²Net has a precise reconstruction of the underlying low-frequency component of the convergence field.

At each smoothing level, we quantify our improvement by

$$\text{Imp} = (\text{RMSE}_i - \text{RMSE}_{\text{MIU}^2\text{Net}}) / \text{RMSE}_i, \quad (30)$$

where RMSE_i is the RMSE of a reconstruction method. Without smoothing, MIU²Net is Imp = 83% better than KS, and Imp = 5% better than UNet. With 1 arcmin smoothing applied, KS is significantly improved, and MIU²Net offers Imp = 34% improvement over KS, and Imp = 38% improvement over UNet. MIU²Net achieves similar levels of improvement to WF, and MCA. MIU²Net also consistently outperforms UNet on RMSE despite both being MMSE estimators. Changing the network structure and regularising in the frequency domain are therefore effective techniques for mass inversion.

5.6 Generalization Across Cosmologies

In this section, we show MIU²Net's ability to generalize across cosmologies despite being trained on a single cosmology. As outlined in Sect. 4.1, we trained our network with $\sigma_8 = 0.82$, $\Omega_m = 0.28$, $\Omega_\Lambda = 0.72$, $\Omega_b = 0.046$, $h = 0.70$, and $n_s = 0.96$. We generate another 500 shear-convergence pairs with our simulation using $\sigma_8 = 0.81$, $\Omega_m = 0.31$, $\Omega_b = 0.049$, $\Omega_c = 0.26$, $\Omega_\nu = 0.0014$, $h = 0.68$, and $n_s = 0.97$ (fiducial in Chen et al. (2025)). We use our trained MIU²Net model to directly predict convergence maps without fine-tuning.

Fig. 9 shows the power spectrum reconstruction for the second cosmology. In the top panel, we show the radial-averaged power spectrum for the new cosmology in black

dashed line, and the old one in black dotted line. Note that the graph is a log-log plot, and the power spectrum difference between the two cosmologies is significant, reaching 19% at the greatest. The lower panel shows the residual power spectrum for the original cosmology in black dotted line. Although we trained MIU²Net on the original cosmology and regularised it with the dotted power spectrum, MIU²Net is able to move away from the trained power spectrum and progress significantly closer to the new truth (black dashed line in both panels). Note that the power spectrum under the new cosmology has higher energy across all frequencies, and it is uncommon for an MMSE estimator to risk a prediction with high energy, especially when regularised on a power spectrum with lower energy. This demonstrates that the MSE term in our loss function is powerful enough to bring up the power spectrum when needed, and our joint loss function is beneficial for both MSE minimisation and power spectrum estimation. Compared to WF and MCA with the correct cosmology as inputs, MIU²Net reaches the same accuracy in intermediate spatial frequencies and better accuracies in low and high spatial frequencies. Quantitatively, MIU²Net achieves 10.8% power spectrum accuracy across all frequency ranges when regularised on a different cosmology, 390% better than Wiener filtering and 350% better than MCALens at $l \simeq 500$. In real observational scenarios, we can retrain MIU²Net if we know the convergence power spectrum. We expect to reach the same 4% uncertainty as in Sect. 5.4 assuming MIU²Net is trained on the correct power spectrum. The input signal power spectrum can be estimated in the same way as for Wiener filtering without impacting the reconstruction result.

For other statistics, Fig. 10 shows that MIU²Net's reconstruction RMSE under different smoothing conditions is almost unchanged, demonstrating that MIU²Net reliably reconstructs the bulk characteristics of the convergence maps and maintains the same level of improvement over other methods. Additionally, we show in Fig. 5 and Fig. B.4 that the correction factor for reconstructing mean convergence generalizes very well across different cosmologies. In the future, we aim to improve our simulation so that MIU²Net is trained on a variety of cosmologies, so that the regularisation is not skewed to a single power spectrum. With our current implementation, however, MIU²Net already generalizes reliably across cosmologies despite being trained on a single, arbitrary cosmology.

5.7 Full MIU²Net Results

Throughout the paper, we have only added shape noise to shear fields for clearer comparisons between MIU²Net and established methods. However, data mask is another im-

portant observational constraint on shear that introduces significant systematics to mass inversion. Masks due to complicated survey geometry, bright stars, cosmic rays, and other observational effects can significantly impact the reconstruction quality. In this section, we include both shape noise and data masks on shear fields and demonstrate MIU²Net’s ability to recover the correct summary statistics when both limitations are present. Importantly, we have not retrained our model, but only added the extra limitations during model inference. We show a typical training data realization with both limitations in the bottom right panel of Fig. 11. MIU²Net can be further extended and customized by using survey-specific data masks, PSF uncertainties, and other systematic in the augmentation pipeline for training data.

Traditionally, different inpainting methods are used to fill the regions where data is missing. One popular inpainting method uses the Discrete Cosine Transform (DCT), as in Pires et al. (2009, 2020). Because the convergence map κ is sparse in DCT space, the strongest DCT coefficients encompass most of the signal, with smaller DCT coefficients describing the effects of noise and missing data. An iterative algorithm can then be used to estimate and enforce a convergence power spectrum in regions of missing data (e.g., Seitz & Schneider 1995; Jullo et al. 2014). In this section, we test MIU²Net ability on masked data by inferring on shear maps with $\sim 20\%$ pixels set to 0, as shown in the bottom left panel of Fig. 11. The sizes and shapes of those masks roughly correspond to bright star distributions. MIU²Net naturally synthesizes information from all map regions to estimate the power spectrum. Because of RAPS loss, the masked regions are automatically inpainted with values following the convergence power spectrum, together with highly sophisticated considerations for border and near-field pixels. MIU²Net thus treats data masks in a similar vein as DCT, but simpler to implement and much quicker as it does not involve iterations once trained.

The difference between shear and reduced shear is another important systematic in mass inversion. According to Eq. (6), there is a linear relation between the shear field γ and the convergence field κ . We have the observable in the form of reduced shear $g = \gamma/(1 - \kappa)$ where $g \simeq \gamma$ for most weak lensing regions. However, for small angular scales and regions near convergence peaks, κ is not negligible and the linear relation in (6) breaks down (White 2005; Shapiro 2009). Variants of traditional methods like KS+ (Pires et al. 2020) use an iterative scheme to estimate the convergence map. In the case of MIU²Net, training with reduced shear instead of shear is theoretically beneficial. On the one hand, MIU²Net does not assume a linear inverse problem but directly learns the mapping, so it is not restricted to a linear reconstruction as KS or WF.

On the other hand, using the reduced shear g almost always leads to a higher SNR because κ is positive in most regions. For regions near convergence peaks, the boost in SNR is the most prominent, leading to better reconstruction for non-linear structures in the mass density field. In principle, the stronger the discrepancies between shear and reduced shear, the better MIU²Net recovers non-Gaussian summary statistics. For fair comparisons, we have not included the reduced shear correction in training MIU²Net. However, it is easy to incorporate reduced shear and further improve the reconstruction quality by augmenting the training set with equation (8).

We show the results of full MIU²Net with shape noise and data masks in Appendix B. Figures B.1–B.7 demonstrate that the MIU²Net reconstructions almost do not degrade compared to MIU²Net with only shape noise. Fig. B.1 and Fig. B.3 show that the reconstruction for peak centroids and amplitudes is accurate, despite the convergence peak about to fall into a masked area. Fig. B.2 illustrates that MIU²Net reconstructions still recover the true dynamic range with minimal scatter. On the mass-sheet degeneracy, MIU²Net reconstructions again reflect the correct mean convergence (Fig. B.4) with the same correction factor $\mu_{\text{ms}} = 1.672$, and remain robust under the second cosmology in the right panel of Fig. B.4. The convergence KDE curves in Fig. B.5 show MIU²Net’s ability to reproduce the (normalized) true convergence distribution even with $\sim 20\%$ of masked data. We plot the power spectrum in Fig. B.6 and show that MIU²Net’s constraint on the power spectrum is almost unchanged, achieving 4% uncertainties over all scales $0 < l \lesssim 500$. KS and WF, however, greatly suffer from missing data and the non-linear relationship between reduced shear and convergence. In Fig. B.7, we show that reconstruction RMSE under all limitations is not significantly different from the shape-noise-only RMSE in Fig. 8. In all tests and summary statistics, MIU²Net achieves comparable results with minimal degradation. This versatility against different forms of observational constraints far exceeds traditional methods where individual iterative algorithms have to be developed to treat each term deviating from the ideal assumption. More complicated dependencies (e.g. how reduced shear with PSF uncertainties influence convergence) that are difficult to solve inversely can now be learned by MIU²Net by simply forward-modelling them in the training set. We can easily customize MIU²Net by connecting the training set to mock galaxy catalogues and other survey-specific simulations as well.

6 CONCLUSION

In this work, we develop MIU²Net, a versatile deep learning framework for weak lensing mass inversion. To reg-

ularise our reconstruction, we construct a combined loss function to jointly estimate a pixel-wise convergence map and its frequency-domain power distribution, recovering the convergence power spectrum with 4% uncertainties up to very small angular scales $l \simeq 500$. In addition to two-point statistics, MIU²Net accurately recovers the convergence distribution, peak centroid, and peak amplitude. The recovered convergence maps also follow the true log-normal distribution with an extended high-end tail. MIU²Net is versatile against different forms of systematics such as shape noise, reduced shear, and data masks. Compared with unsupervised methods such as Kaiser-Squires, Wiener filtering, and MCALens, as well as supervised learning-based methods such as DeepMass, MIU²Net achieves superior reconstruction quality and better error handling in all metrics and summary statistics. MIU²Net is also able to generalize across cosmologies despite being trained on a fixed cosmology.

In the era of Stage IV surveys, many large-scale weak lensing projects are joining forces, among which are the Chinese Space Station Telescope (CSST; Zhan 2011, 2021; Yao et al. 2024), *Euclid* (Laureijs et al. 2011), Vera Rubin Observatory’s Legacy Survey of Space and Time (LSST; Ivezić et al. 2019), and the Nancy Grace Roman Space Telescope (Akeson et al. 2019). With massive sky coverage and high galaxy density, these surveys will provide us with unprecedented weak lensing data. MIU²Net is well-positioned to significantly contribute to the construction of mass maps from these future surveys. Although the error on power spectrum is yet insufficient to constrain cosmological parameters using convergence maps, we demonstrate that power spectrum regularisation is effective and our deep learning algorithm is versatile for accurate mapping of convergence distribution. MIU²Net can open many possibilities, including dark matter halo identification, statistics, and studies on galaxy evolution under different dark matter environments. By generating precise dark matter mass distributions, our method will not only become an essential tool for dark matter mass mapping but also provide valuable insights into the interplay between the baryonic world and the dark matter universe.

Acknowledgements We thank Mingxiang Fu for managing the GPU server, and Yufei Meng for useful discussions. The cosmological simulations were mainly conducted on the Yunnan University Astronomy Supercomputer. RL acknowledges the support by National Key R&D Program of China No. 2022YFF0503403, the support of National Nature Science Foundation of China (Nos. 11988101), the support from the Ministry of Science and Technology of China (Nos. 2020SKA0110100), the science research grants from the China Manned Space Project (Nos. CMS-CSST-2025-A03), CAS Project for Young Scientists in

Basic Research (No. YSBR-062), and the support from K.C.Wong Education Foundation. XL acknowledges support from the NSFC of China under grants No. 12173033 and No. 11803028, National Key R&D Program of China No. 2022YFF0503403, YNU grant No. C176220100008, and the research grants from the China Manned Space Project No. CMS-CSST-2021-B01.

All PYTHON code and data that we used to generate the figures in the paper are available at <https://github.com/MIU2NET/miu2net>. We have also included all 500 convergence maps reconstructed independently by MIU²Net, KS, and WF, which are used to generate the figures. The majority of KS and WF reconstruction code are adapted from the publicly available `cosmostat` package at <https://github.com/CosmoStat/cosmostat>.

References

Akeson, R., Armus, L., Bachelet, E., et al. 2019, arXiv e-prints, arXiv:1902.05569 15
 Alsing, J., Heavens, A., & Jaffe, A. H. 2017, MNRAS, 466, 3272 5
 Bartelmann, M., & Schneider, P. 2001, Phys. Rep., 340, 291 2
 Blau, Y., & Michaeli, T. 2018, in Proceedings of the IEEE conference on computer vision and pattern recognition, 6228 7
 Bradač, M., Lombardi, M., & Schneider, P. 2004, A&A, 424, 13 2, 4, 9
 Chen, Z., Yu, Y., Han, J., & Jing, Y. 2025, Science China Physics, Mechanics, and Astronomy, 68, 289512 13
 Clerkin, L., Kirk, D., Manera, M., et al. 2017, MNRAS, 466, 1444 9
 Cremonese, P., Ezquiaga, J. M., & Salzano, V. 2021, Phys. Rev. D, 104, 023503 9
 Davies, C. T., Cautun, M., Giblin, B., et al. 2021, MNRAS, 507, 2267 1
 Davies, C. T., Cautun, M., & Li, B. 2018, MNRAS, 480, L101 1
 Deria, E., Starck, J. L., & Pires, S. 2012, A&A, 540, A34 2
 Elad, M., Kawar, B., & Vaksman, G. 2023, SIAM Journal on Imaging Sciences, 16, 1594 7
 Falco, E. E., Gorenstein, M. V., & Shapiro, I. I. 1985, ApJ, 289, L1 2, 4
 Fiedorowicz, P., Rozo, E., Boruah, S. S., Chang, C., & Gatti, M. 2022, MNRAS, 512, 73 2
 Hamana, T., Shirasaki, M., Miyazaki, S., et al. 2020, PASJ, 72, 16 10
 Hikage, C., Oguri, M., Hamana, T., et al. 2019, PASJ, 71, 43 10
 Hilbert, S., Hartlap, J., & Schneider, P. 2011, A&A, 536, A85 9

Hilbert, S., Hartlap, J., White, S. D. M., & Schneider, P. 2009, *A&A*, 499, 31 6

Hildebrandt, H., Viola, M., Heymans, C., et al. 2017, *MNRAS*, 465, 1454 10

Hong, S. E., Park, S., Jee, M. J., Bak, D., & Cha, S. 2021, *ApJ*, 923, 266 2

Isola, P., Zhu, J.-Y., Zhou, T., & Efros, A. A. 2017, in *Proceedings of the IEEE conference on computer vision and pattern recognition*, 1125 2

Ivezić, Ž., Kahn, S. M., Tyson, J. A., et al. 2019, *ApJ*, 873, 111 15

Jain, B., Seljak, U., & White, S. 2000, *ApJ*, 530, 547 9

Jasche, J., & Wandelt, B. D. 2013, *MNRAS*, 432, 894 2

Jeffrey, N., Lanusse, F., Lahav, O., & Starck, J.-L. 2020, *MNRAS*, 492, 5023 2, 6, 7, 8

Jeffrey, N., Abdalla, F. B., Lahav, O., et al. 2018, *MNRAS*, 479, 2871 2

Jeffrey, N., Gatti, M., Chang, C., et al. 2021, *MNRAS*, 505, 4626 5, 10

Joachimi, B., Semboloni, E., Hilbert, S., et al. 2013, *MNRAS*, 436, 819 11

Jullo, E., Pires, S., Jauzac, M., & Kneib, J. P. 2014, *MNRAS*, 437, 3969 8, 14

Kaiser, N., & Squires, G. 1993, *ApJ*, 404, 441 2, 4

Lahav, O., Fisher, K. B., Hoffman, Y., Scharf, C. A., & Zaroubi, S. 1994, *ApJ*, 423, L93 2, 5

Lanusse, F., Starck, J. L., Leonard, A., & Pires, S. 2016, *A&A*, 591, A2 2, 8, 10

Laureijs, R., Amiaux, J., Arduini, S., et al. 2011, arXiv e-prints, arXiv:1110.3193 15

LeCun, Y., Boser, B., Denker, J., et al. 1989, *Advances in neural information processing systems*, 2 5

Ling, C., Wang, Q., Li, R., et al. 2015, *Phys. Rev. D*, 92, 064024 1

Liu, J., & Madhavacheril, M. S. 2019, *Phys. Rev. D*, 99, 083508 1

Liu, X., Pan, C., Li, R., et al. 2015, *MNRAS*, 450, 2888 1

Liu, X., Li, B., Zhao, G.-B., et al. 2016, *Phys. Rev. Lett.*, 117, 051101 1

Mandelbaum, R. 2018, *ARA&A*, 56, 393 2

Mandelbaum, R., Miyatake, H., Hamana, T., et al. 2018, *PASJ*, 70, S25 4

Mead, J. M. G., King, L. J., & McCarthy, I. G. 2010, *MNRAS*, 401, 2257 1

Pires, S., Starck, J. L., Amara, A., et al. 2009, *MNRAS*, 395, 1265 2, 4, 8, 14

Pires, S., Vandenbussche, V., Kansal, V., et al. 2020, *A&A*, 638, A141 1, 2, 4, 8, 11, 14

Porqueres, N., Heavens, A., Mortlock, D., & Lavaux, G. 2021, *MNRAS*, 502, 3035 2

Price, M. A., McEwen, J. D., Pratley, L., & Kitching, T. D. 2021, *MNRAS*, 500, 5436 2

Qin, X., Zhang, Z., Huang, C., et al. 2020, *Pattern recognition*, 106, 107404 6, 8

Rexroth, M., Natarajan, P., & Kneib, J.-P. 2016, *MNRAS*, 460, 2505 9

Ronneberger, O., Fischer, P., & Brox, T. 2015, in *Medical image computing and computer-assisted intervention—MICCAI 2015: 18th international conference, Munich, Germany, October 5-9, 2015, proceedings, part III* 18, Springer, 234 6

Schneider, P., & Seitz, C. 1995, *A&A*, 294, 411 2, 4

Seitz, C., & Schneider, P. 1995, *A&A*, 297, 287 8, 14

Seitz, C., & Schneider, P. 1997, *A&A*, 318, 687 4, 9

Shapiro, C. 2009, *ApJ*, 696, 775 4, 14

Shirasaki, M., Yoshida, N., & Ikeda, S. 2019, *Phys. Rev. D*, 100, 043527 2, 10, 11

Simon, P., Taylor, A. N., & Hartlap, J. 2009, *MNRAS*, 399, 48 5

Starck, J. L., Themelis, K. E., Jeffrey, N., Peel, A., & Lanusse, F. 2021, *A&A*, 649, A99 2, 8

Tam, S.-I., Massey, R., Jauzac, M., & Robertson, A. 2020, *MNRAS*, 496, 3973 1

Troxel, M. A., MacCrann, N., Zuntz, J., et al. 2018, *Phys. Rev. D*, 98, 043528 10

van Waerbeke, L. 2000, *MNRAS*, 313, 524 4

Wandelt, B. D., Larson, D. L., & Lakshminarayanan, A. 2004, *Phys. Rev. D*, 70, 083511 5

White, M. 2005, *Astroparticle Physics*, 23, 349 4, 14

Yao, J., Shan, H., Li, R., et al. 2024, *MNRAS*, 527, 5206 15

Zaroubi, S., Hoffman, Y., Fisher, K. B., & Lahav, O. 1995, *ApJ*, 449, 446 2, 5

Zhan, H. 2011, *Scientia Sinica Physica, Mechanica & Astronomica*, 41, 1441 15

Zhan, H. 2021, *Chinese Science Bulletin*, 66, 1290 15

Appendix A: TRAINING SPECIFICATIONS

We detail our training specifications and hyperparameters for MIU²Net in Table A.1. The full model takes ~ 1.5 minutes per epoch to train on one NVIDIA A100 GPU, and the validation loss usually plateaus after ~ 256 epochs. However, slightly better results may be achieved with greater batch size and more training epochs. Below, we show the hyperparameters used to train the specific model analyzed in this paper.

Appendix B: ADDITIONAL FIGURES

Table A.1 Training specifications for MIU²Net.

Name	Symbol	Value	Notes
epoch	e	2000	Total training epochs. Training usually plateaus after ~ 256 epochs and has very little improvement afterwards.
batch size	b	128	Batch size used to train the final model. Any batch size greater than 16 achieves comparable results.
learning rate	lr	1×10^{-4}	Initial learning rate. This learning rate is adjusted every epoch following a cosine annealing schedule with a final learning rate of 1×10^{-10} .
alpha	α	1.0	Weight for MSE loss; see equation (25).
beta	β	3.0	Weight for RAPS Loss; see equation (25).
cutoff radius	r_{\max}	16.0	Cutoff radius for RAPS loss in units of pixel; see Eq. (28).
weight decay	wd	0	Weight decay for AdamW optimizer.
delta	δ	50.0	The threshold where Huber loss changes between MSE loss and l_1 loss. During training, we use Huber loss instead of plain MSE loss for the MSE term l_{MSE} to prevent gradient explosion in the very first few training steps. A very high delta ensures Huber loss to be identical to MSE loss once training stabilizes.
galaxy number	n_g	20.0	Number of galaxies per square arcmin used to estimate shape noise.
mask fraction	mf	0 – 25%	Fraction of pixels to be masked in an input shear or reduced shear map. Percentage randomized every training step.

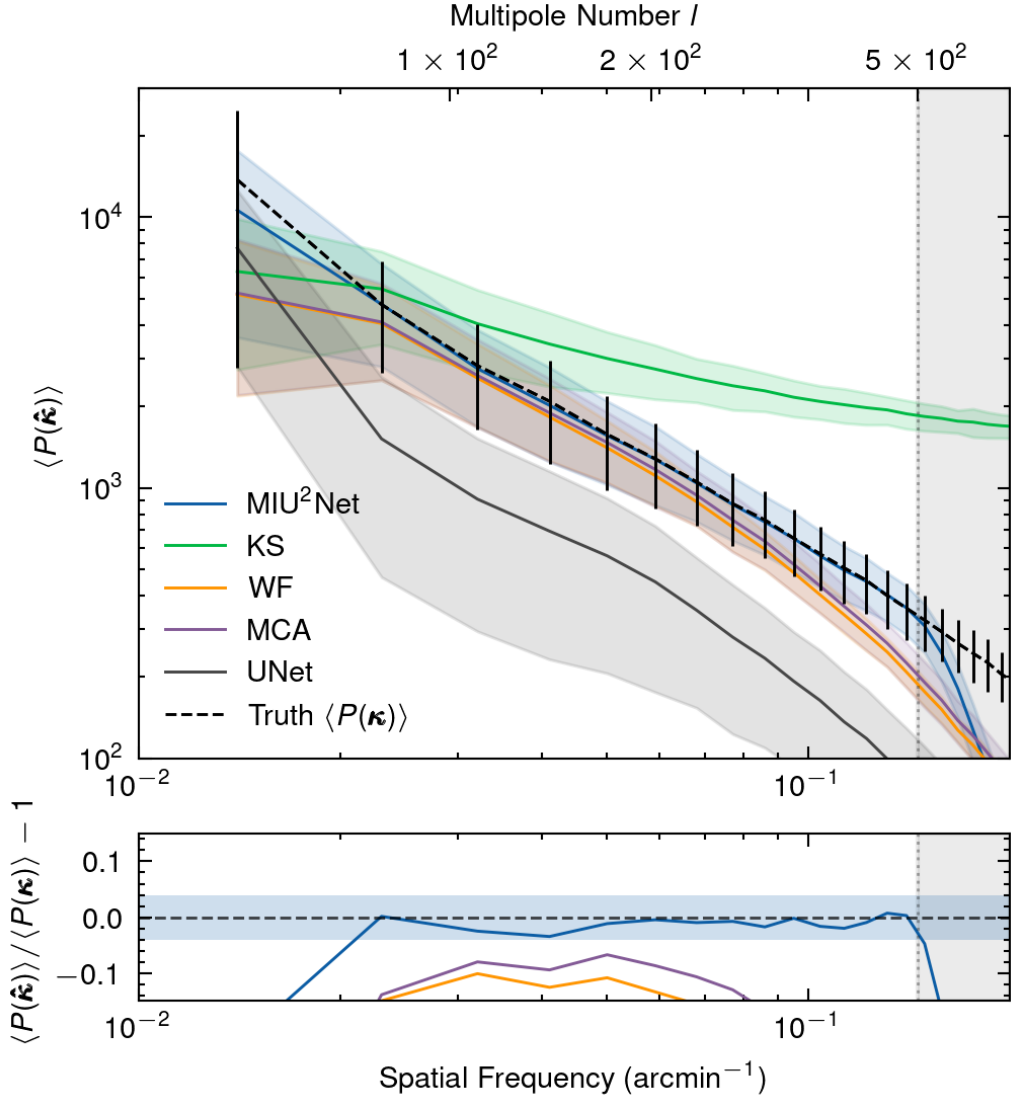


Fig. 7 Power spectrum comparison. *Top panel*: radial-averaged power spectra for truth, MIU²Net, KS, WF, MCA, and UNet. The black dashed line and error bars show the mean and the standard deviation of the true power spectrum for 500 realizations. For each of the reconstruction methods, the coloured lines show the mean power spectrum $\langle P(\hat{\kappa}) \rangle$ and the shadings mark the respective standard deviation. The grey vertical dotted line denotes the cutoff r_{\max} for MIU²Net's RAPS loss, and the grey region to the right corresponds to high frequencies *not* included in our implementation of RAPS loss. MIU²Net power spectrum closely follows the true mean and standard deviation within the range of RAPS loss. The discrepancies between the true power spectrum and all recovered power spectra at the lowest frequency bin can be partly attributed to the imperfect recovery of the DC component, i.e. mean convergence. At high frequencies going into the grey region, the power spectrum for MIU²Net rapidly diverges from the truth, as those frequencies are not considered in our loss function. Choosing different cutoff radii r_{\max} in the frequency domain changes the extent of the grey region. *Bottom panel*: residual power spectra for each reconstruction method with respect to the truth. The coloured lines correspond to the same label in the top panel, but KS, and UNet are now out of the plot range. The blue band bounds the region $[-0.04, 0.04]$ where most of the MIU²Net residual power spectrum resides. Note that MIU²Net slightly underestimates the power at almost all frequencies, but it always stays within the ±4% uncertainty band except at the lowest frequency bin.

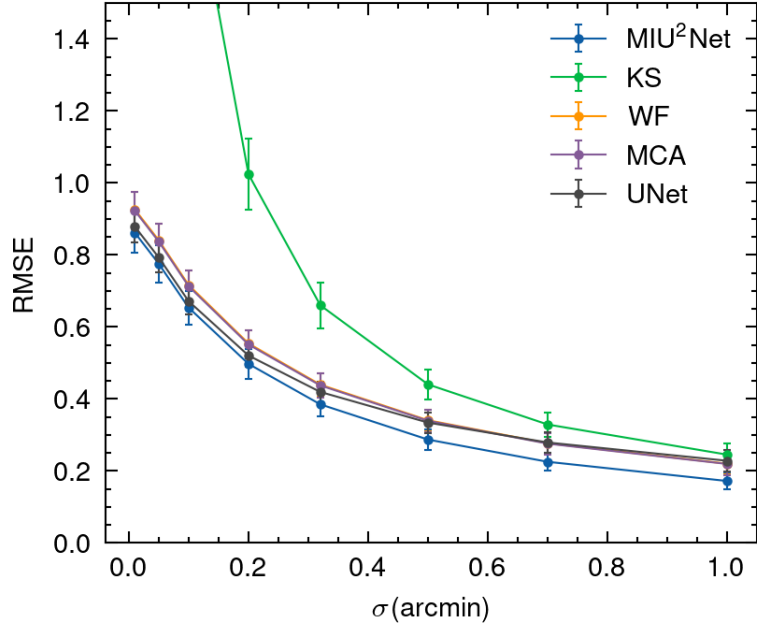


Fig. 8 Root Mean Square Error (RMSE) under different smoothing conditions for each reconstruction method. Error bars denote one standard deviations. It is clear that MIU²Net significantly outperforms all other methods across all smoothing scales.

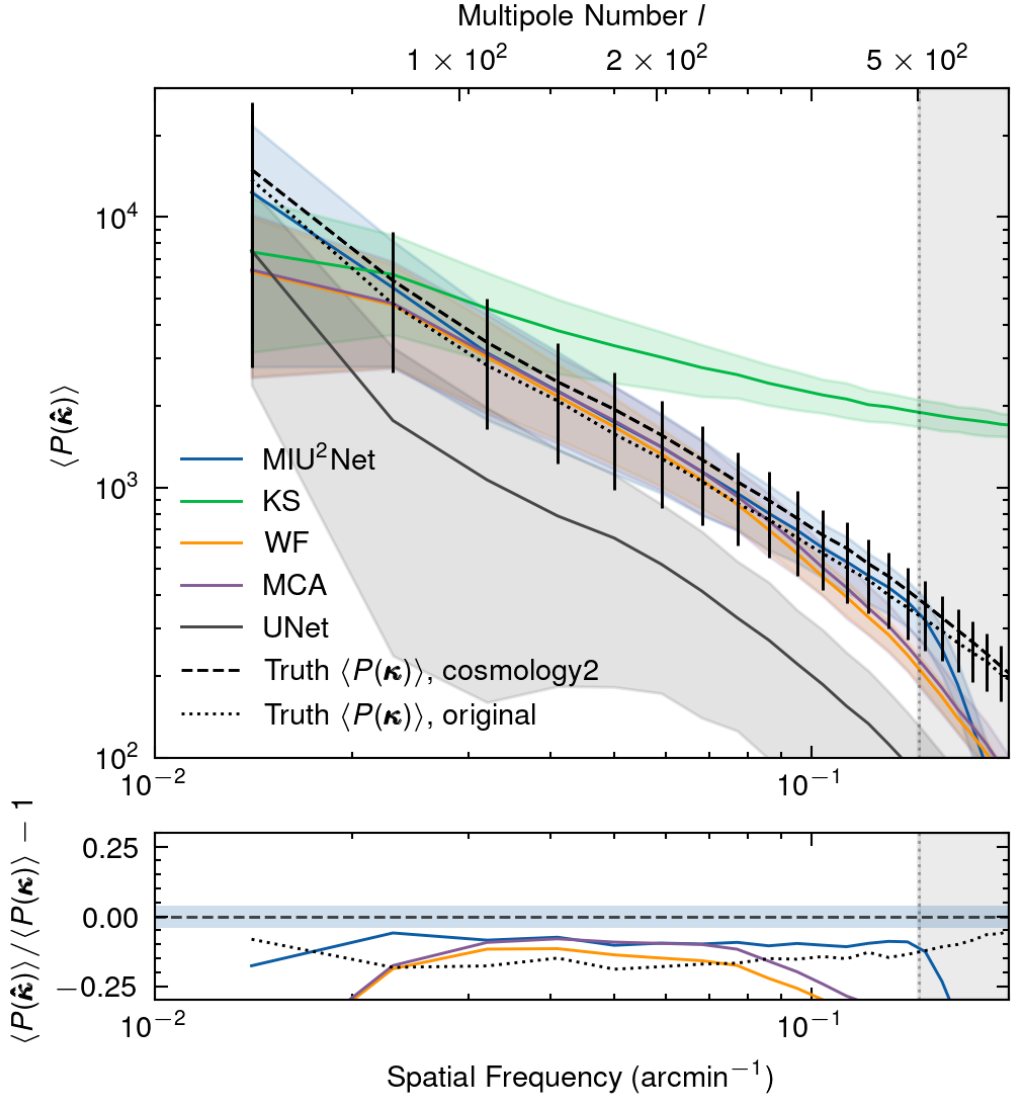


Fig. 9 Power spectrum comparison for the second cosmology. *Top panel*: radial-averaged power spectra for truth (new test cosmology), truth (original trained cosmology), MIU 2 Net, KS, WF, MCA, and UNet. The black dashed line and the error bars show the mean and the standard deviation for the true power spectrum for 500 realizations, under the new cosmology. The black dotted line shows the true power spectrum for the original power spectrum. Other coloured lines and shaded areas follow the same conventions in Fig. 7. There is a significant difference between the power spectra for the two cosmologies. *Bottom panel*: residual power spectra for each reconstruction method with respect to the truth. The black dotted line shows the residual power spectrum of the original cosmology with respect to the new one. The blue band bounds the same region $[-0.04, 0.04]$ as in Fig. 7. Although trained on a different cosmology, MIU 2 Net reaches the same performance as MCA (with the correct power spectrum as input) in intermediate spatial frequencies, and outperforms all methods in low and high spatial frequencies. Notably, MIU 2 Net deviates from the trained dotted line and move closer to the true power spectrum.

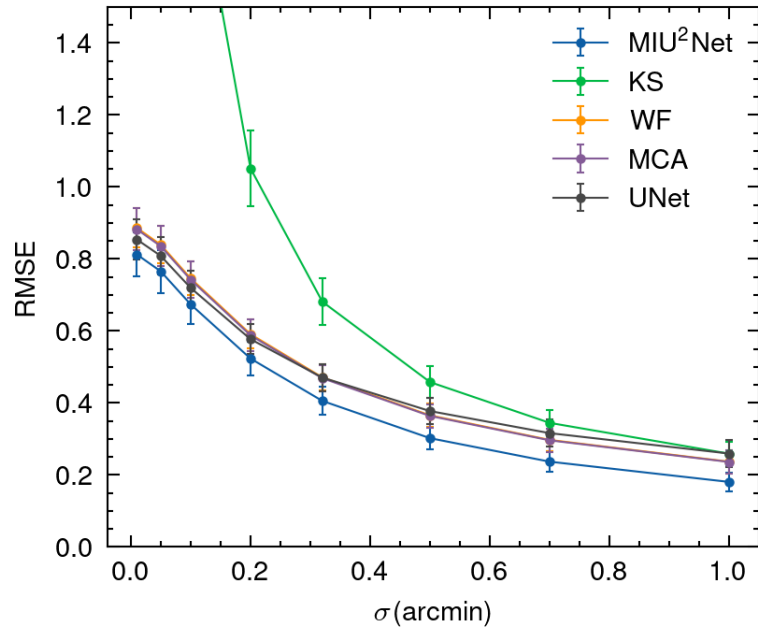


Fig. 10 Root Mean Square Error (RMSE) under different smoothing conditions for the second cosmology. There is no significant difference between Fig. 8 and RMSE with a different cosmology.

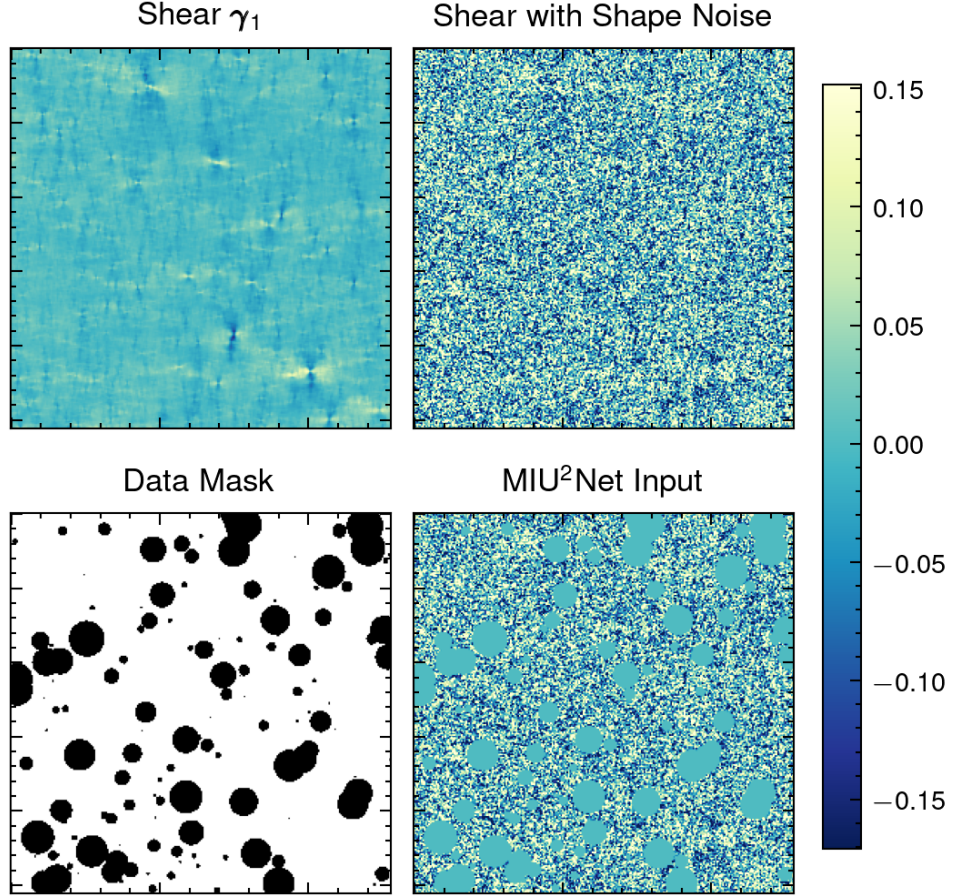


Fig. 11 Visual comparison between shear, reduced shear, data mask, and MIU²Net input data. *Top left panel*: first component of a noiseless shear map γ_1 . *Top right panel*: the same first component of the shear field, with an added shape noise corresponding to $n_g = 20 \text{ arcmin}^{-2}$. *Bottom left panel*: one mask realization covering $\sim 20\%$ of the pixels in the map. Note that the coverage percentage is randomized during training. *Bottom right panel*: the shear field with data mask and shape noise corresponding to $n_g = 20 \text{ arcmin}^{-2}$. The masked regions are set to 0. This is what the full MIU²Net sees as its input (in the first channel; the second channel is the second component of noisy, masked reduced shear). We draw a new data mask realization and a shape noise realization for every training step.

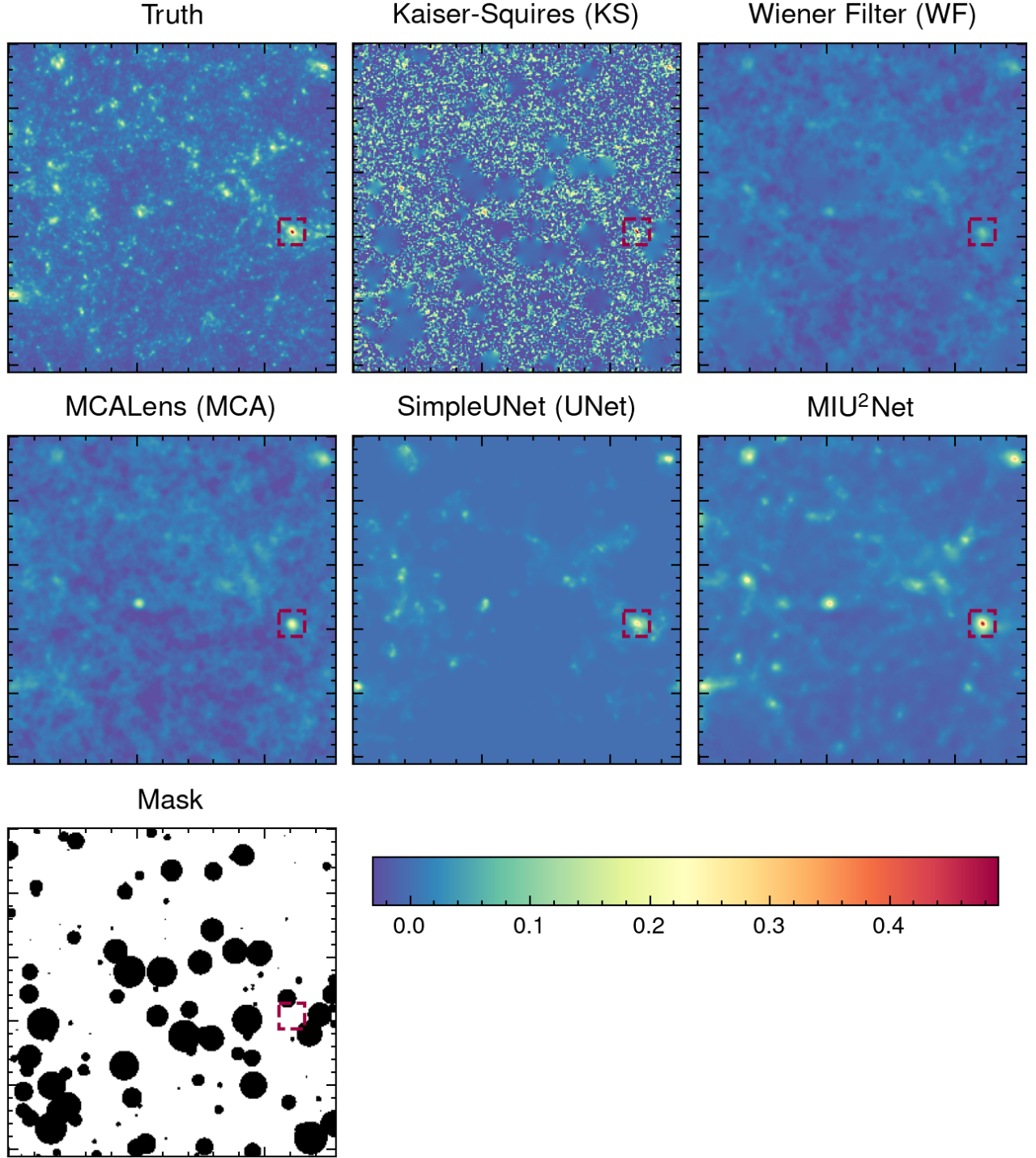


Fig. B.1 Visual comparison between Truth, KS, WF, MCA, UNet, and MIU²Net convergence map reconstructed from a masked noisy shear field. The underlying noiseless shear is the same realization as in Fig. 1. We can see the shape of the data mask in the blue-green circular regions in the KS reconstruction, because KS does not handle noise or data masks. We visualize in detail the scarlet dashed square region in each panel (the same regions as in Fig. 1) in Fig. B.3. Note that the central peak in the scarlet square falls right into a masked area.

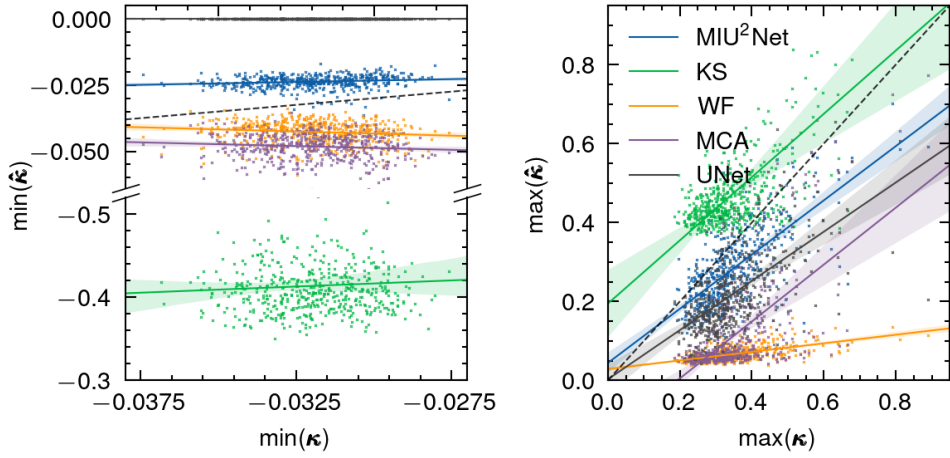


Fig. B.2 Dynamic range comparison for MIU²Net, KS, WF, MCA, and UNet under shape noise and data masks. *Left panel*: we plot the same minimum predicted convergence value $\min(\hat{\kappa})$ against minimum true convergence value $\min(\kappa)$ for each reconstruction, as in Fig. 3. We also include the best-fit line and 95% confidence interval. MIU²Net accurately recovers the lower bound. *Right panel*: scatter plot, best-fit line, and 95% confidence interval for maximum values for each truth-prediction pair. Despite the increased noise in input maps, the best-fit line for MIU²Net is the closest to the ideal reconstruction of the upper bound.

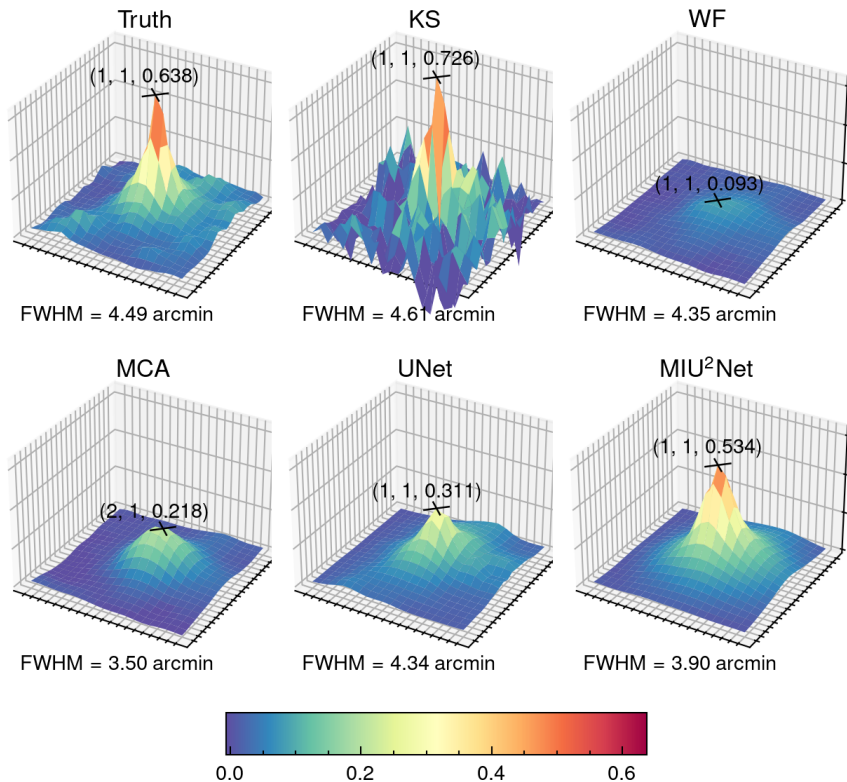


Fig. B.3 Parallel to Fig. 4, we plot the centroid and amplitude for an individual convergence peak under shape noise and data masks. The plotted regions correspond to the scarlet dashed square regions in Fig. B.1. Note that the true peak centroid is very close to a masked region in the shear map. Both MIU²Net and UNet recover a peak, but MIU²Net has an amplitude closer to the truth.

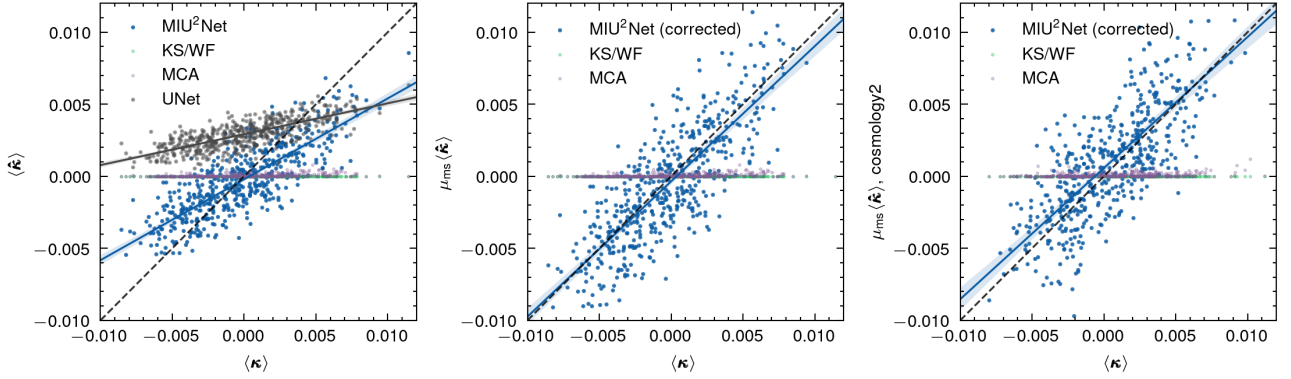


Fig. B.4 Mean convergence plot with shape noise and masked regions present in the reconstruction. We use the same correction factor $\mu_{\text{ms}} = 1.672$ as in Fig. 5 in the middle panel. MIU²Net reconstructions still follow the ideal linear relationship (black dashed line) with the correction factor based on 0% masked fraction. In the right panel, we plot the mean convergence based on the second cosmology with both systematics.

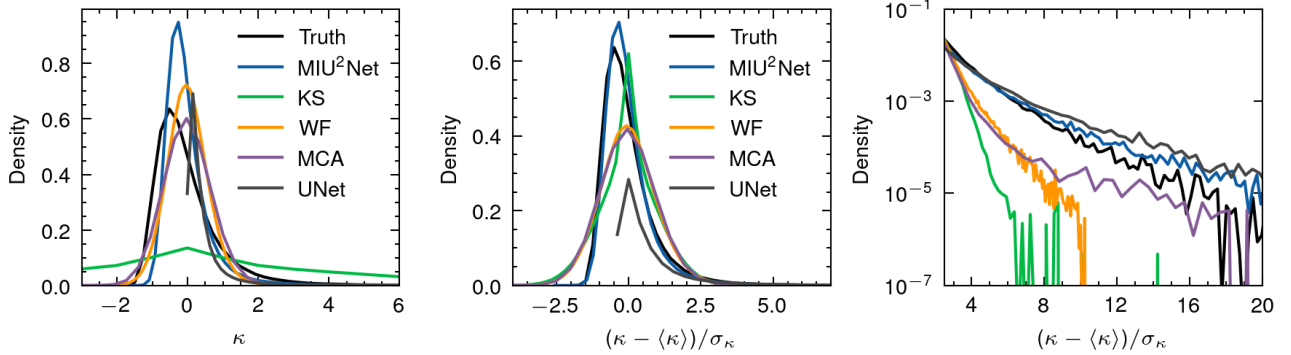


Fig. B.5 Kernel Density Estimation (KDE) showing the convergence distribution for all methods under shape noise and data masks covering $\sim 20\%$ of all pixels in the input maps. As shown in the middle panel and the right panel, MIU²Net reproduces the true log-normal distribution with an extended high-end tail, whereas KS and WF significantly deviate from the true distribution. The shape of the MIU²Net KDE curve is almost unchanged as in Fig. 6, demonstrating MIU²Net's versatility against $\sim 20\%$ of missing data.

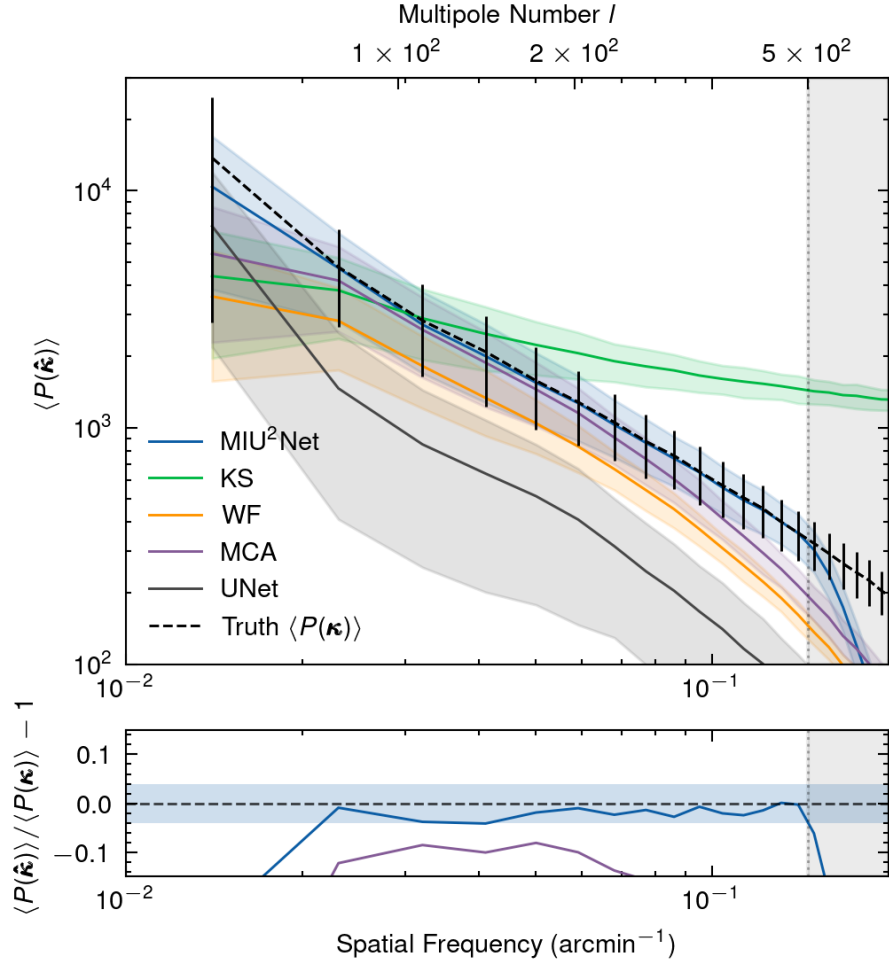


Fig. B.6 Radial-averaged power spectrum for each method under shape noise and data masks. Compared to Fig. 7, the MIU²Net power spectrum is almost unchanged, achieving 4.0% uncertainties over all scales $0 < l \lesssim 500$. In the bottom panel, all other methods are outside of the plot range except MCA. The blue band in the bottom panel bounds the same $\pm 4\%$ uncertainty region as in Fig. 7. KS and WF power spectra degrade noticeably under missing data and the non-linear relationship between reduced shear and convergence. At $l \simeq 500$, MIU²Net now achieves 1370% improvement over WF (assuming 4% error for MIU²Net).

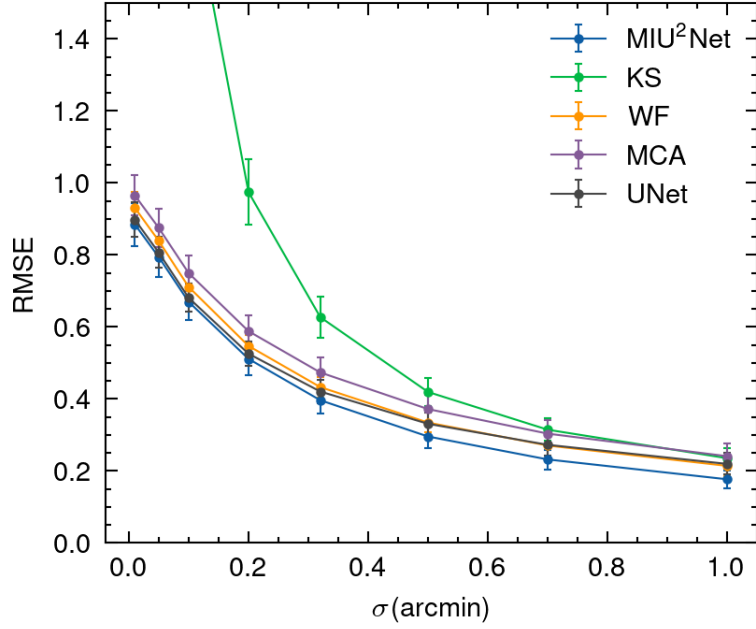


Fig. B.7 Root Mean Square Error (RMSE) under different smoothing conditions, under shape noise, reduced shear, and data mask. There is no significant difference between the shape-noise-only RMSE in Fig. 8 and RMSE under all limitations.